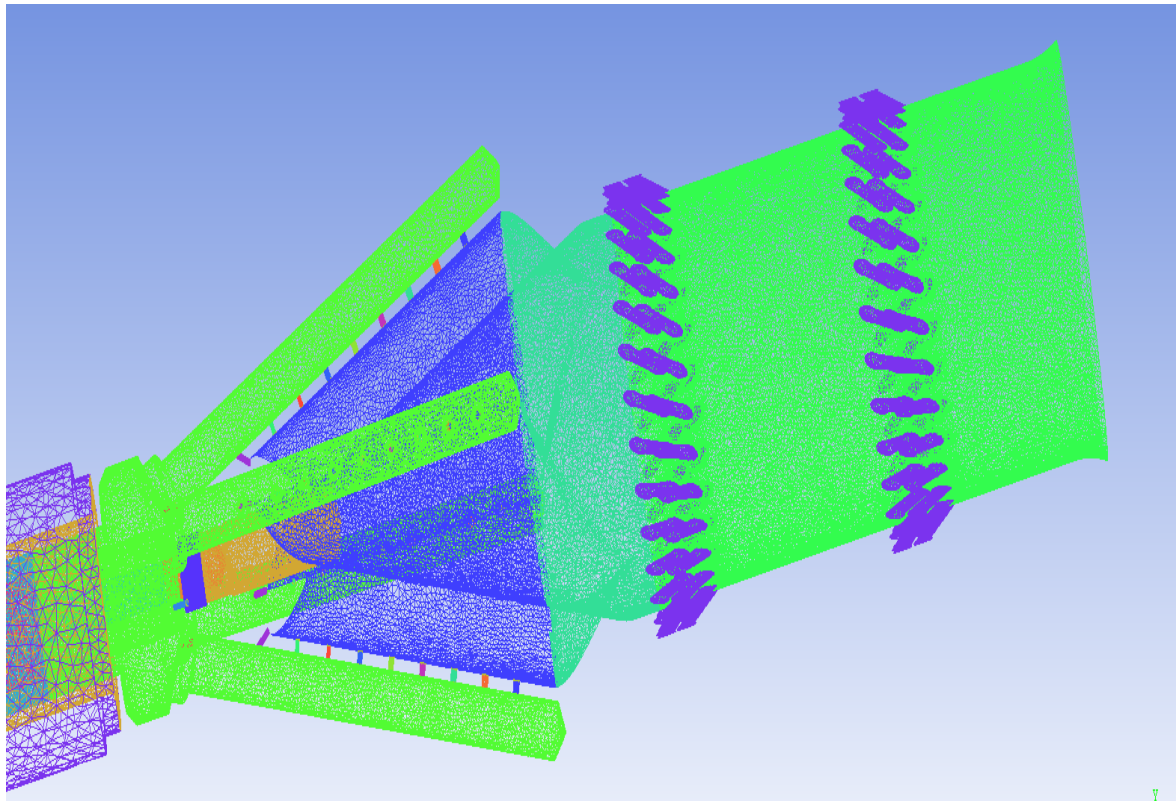


CHALMERS



CFD evaluation of a jet in cross flow related to a gas turbine burner

Master's Thesis in Applied Mechanics

AKRAM SOROUSH

Department of Applied Mechanics
Division of Fluid Mechanics

CHALMERS UNIVERSITY OF TECHNOLOGY
Göteborg, Sweden 2012
Master's thesis 2012:48

MASTER'S THESIS IN APPLIED MECHANICS

CFD evaluation of a jet in cross flow
related to a gas turbine burner

AKRAM SOROUGH

Department of Applied Mechanics
Division of Fluid Mechanics

CHALMERS UNIVERSITY OF TECHNOLOGY

Göteborg, Sweden 2012

CFD evaluation of a jet in cross flow related to a gas turbine burner

AKRAM SOROUSH

© AKRAM SOROUSH, 2012

Master's Thesis 2012:48

ISSN 1652-8557

Department of Applied Mechanics

Division of Fluid Mechanics

Chalmers University of Technology

SE-412 96 Göteborg

Sweden

Telephone: + 46 (0)31-772 1000

Chalmers Reproservice

Göteborg, Sweden 2012

CFD evaluation of a jet in cross flow related to a gas turbine burner

Master's Thesis in Applied Mechanics
AKRAM SOROUSH
Department of Applied Mechanics
Division of Fluid Mechanics
Chalmers University of Technology

ABSTRACT

In order to increase the performance of the burner in the combustor system, the flame behavior has to be understood by studying the flow in the burner. The goal of this thesis is to present an optimized mesh strategy for simulating a jet in cross flow related to the fuel injection nozzle at the burners used in Siemens gas turbines SGT-700 and SGT-800. The optimization is performed in order to acquire the most accurate results with the least number of cells. The approaches in this thesis may be used to improve the fuel-air mixing prediction of the Siemens Industrial Turbomachinery (SIT) burners.

For this purpose the behavior of fluid flow and turbulent mixing in a jet in cross flow is investigated.

The simulations are carried out using ANSYS CFX v. 13.0 and Fluent v. 13.0. The standard and realizable k - ϵ turbulence models are implemented. Since the goal is to find a grid independent solution, Fluent is selected as the main tool due to its grid adaption capability.

The accuracy of the predicted flow parameters, namely velocities and concentration field, is evaluated using experimental data which are obtained by Siemens Energy at Mulheim, Germany and Orlando USA, in collaboration with Karlsruhe University, Germany.

It is shown that by selecting the suitable region for refinement, proper grid resolution in the jet nozzle and considering reasonable channel wall resolution by adding suitable prism layers, accuracy of the results could be improved without unnecessary cell refinement. Also the results confirm the grid independency for velocity profile.

Key words: jet in cross flow, grid independency, mesh optimization, gas turbine burner

Contents

ABSTRACT	I
SAMMANFATTNING	II
CONTENTS	III
PREFACE	VI
NOTATIONS	VII
1 THESIS GOALS	1
1.1 Siemens Industrial Turbomachinery AB (SIT AB)	1
1.2 Gas turbine	1
1.3 Gas turbine burner	1
1.4 Computational Fluid Dynamics (CFD)	2
2 THEORY	3
2.1 Conservation of mass	3
2.2 Conservation of momentum	4
2.3 Conservation of energy	7
2.4 Scalar transport	9
2.5 General transport equations	9
2.6 Reynolds average	9
2.7 Closure problems	10
2.8 Turbulence	11
2.9 Turbulence models	11
2.9.1 Algebraic (Zero-Equation) Models	11
2.9.2 One-Equation Models	12
2.9.3 Two-Equation Models	12
2.10 Law of the wall	13
2.10.1 Near the wall	14
3 METHODOLOGY AND RESULTS	16
3.1 SGT-700/800 burner	16
3.2 Reference case	17
3.2.1 Domain	17
3.2.2 Grid	18
3.2.3 Boundary conditions	19
3.2.4 Experimental set-up	19
3.3 Turbulence modeling	19
3.4 Solvers and models	20

3.5	Parameter study	20
3.6	SIT case	21
3.6.1	Mesh generation	22
3.6.2	Results	23
3.7	Case study I: density boxes along jet trajectory	24
3.7.1	Mesh generation	24
3.8	Case study II: structured grid in nozzle pipe	25
3.8.1	Blocking effect	25
3.8.2	Aligned nodes cases	26
3.8.3	Results	26
3.9	Case study III: Prism layers	28
3.9.1	Prism layers	28
3.9.2	Results	30
3.10	Case study IV: without density boxes	31
3.11	Grid independency	32
3.12	Case study V: grid independent solution for dimensionless concentration	33
3.13	Fluent versus CFX	40
4	CONCLUSION	42
5	FUTURE WORK	44
6	REFERENCES	45
	APPENDIX	46

Preface

This study summarized my work carried out from April to October 2012 at Siemens Industrial Turbomachinery AB in Finspong, Sweden. This master thesis has been done under supervision of Dr.Daniel Loerstad and Dr.Darioush G-Barhaghi as industrial supervisors.

This research is performed as a master thesis in applied mechanics department, division of fluid dynamics, Chalmers University of Technology, Sweden.

I would like to thank my both supervisor Daniel Loerstad and Darioush G-Barhaghi for their valuable supports and guidance through all my work. I learned a lot from them and without their supports this thesis would not be possible. Furthermore I would like to express my gratitude to Anders Häggmark at the division of combustion of Siemens Industrial Turbomachinery who gave me the opportunity to work on this thesis.

I would like to thank Prof. Håkan Nilsson for being the examiner for my thesis work. Last but not least my thanks and appreciations go to my family and friends who had supported me kindly.

Finspong, November 2012

Akram Soroush

Notations

Roman upper case letters

A_s	Circular segment area
C	Dimensionless Concentration
CFD	Computational Fluid Dynamics
D	Jet diameter
DNS	Direct Numerical Simulation
DLE	Dry Low Emission
E	Energy
F	Force
JIC	Jet In Cross flow
k	Thermal conductivity
LES	Large Eddy Simulation
LIF	Laser Induced Fluorescence
P	Pressure
P_k	Turbulence production
P_{kb}	Buoyancy production
PIV	Particle Image Velocimetry
R	Velocity ratio
$RANS$	Reynolds-averaged Navier-Stokes
S_i	Source term
Sc_t	Turbulent Schmidt number
SGT	Siemens Gas Turbine
SIT	Siemens Industrial Turbomachinery
SST	Shear Stress Transport model
U	Mean velocity in x direction
U_{cross}	Maximum mean velocity component U of cross flow at $x/D=-1$
W	Mean velocity in z direction

Roman lower case letter

a	Acceleration
c	Concentration
k	Turbulent kinetic energy
k	Von Kármán constant (equation 2-46)
\dot{m}	Mass flow rate
q_i	Heat flux vector
t	Time
u	Velocity component in x-direction
u^+	Dimensionless velocity
u_τ	Shear velocity
$u'_i u'_j$	Reynolds stress tensor
v	Velocity component in y-direction
w	Velocity component in z-direction

y^+ Distance from the wall measured in u_τ and ν

Greek upper case letters

Γ diffusion coefficient
 Φ Averaged value of any variable

Greek lower case letter

δ Boundary layer thickness
 ε dissipation
 ϕ General variable
 μ Dynamic viscosity
 μ_t Dynamic turbulent viscosity
 \mathcal{G} Turbulent velocity scale
 ℓ Turbulent length scale
 ρ Density
 τ_{ij} Viscous stress tensor
 ν Kinematic viscosity

1 Thesis goals

In order to increase the performance of the burner in the combustor system, the flame behavior has to be understood by studying the flow in the burner. The goal of this project is to present an optimized mesh strategy for simulating a jet in cross flow related to the fuel injection nozzle at the burners used in Siemens gas turbines SGT-700 and SGT-800. The optimization is performed in order to acquire the most accurate results with the least number of cells. The approaches in this thesis may be used to improve the fuel-air mixing prediction for the SIT burners. For this purpose the behavior of fluid flow and turbulent mixing in a jet in cross flow is investigated.

The accuracy of the simulation results is evaluated using experimental data which is obtained by Siemens Energy at Mulheim, Germany and Orlando, USA in collaboration with Karlsruhe University, Germany.

1.1 Siemens Industrial Turbo machinery AB (SIT AB)

Siemens is a multinational company with wide range of products and services worldwide in the energy, healthcare, industry and infrastructure and cities sectors. Siemens Industrial Turbo-machinery in Finspong in Sweden is part of the global Siemens Energy sector which develops, manufactures, sells and installs gas and steam turbines all over the world. Siemens globally manufactures turbines with power range of 5-340 MW and SIT in Sweden is responsible for the range 15-50 MW. [www.siemens.com, Bruneflod (2010)]

1.2 Gas turbine

The gas turbine is the most adaptable kind of turbo-machinery. It can be utilized in different critical industry such as power generation, oil and gas, process plants, aviation and also smaller industries.

Gas turbines regardless of the industry they are used, consist of three main parts; compressor, combustor and turbine. These parts are illustrated in Figure 1.1.

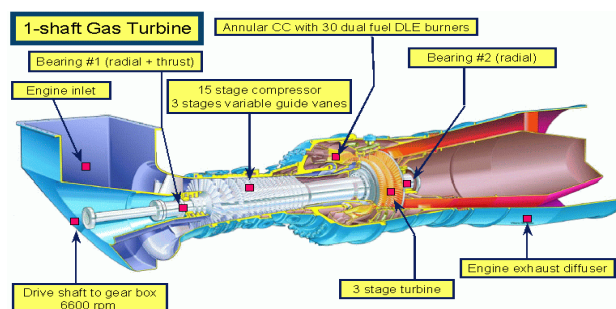


Figure 1.1 Siemens gas turbine SGT- 800

Compressed air from the compressor enters the combustor module. Fuel and air are mixed in burners and then the mixture is ignited in the combustion chamber. The reactive gases expands due to the heat from the combustion chemical reactions and the flue gases flow through the turbine part which drives the compressor shaft and the

rest of the power can be used for driving the power shaft for electricity generation or other mechanical drive.

1.3 Gas turbine burner

One of the main parts of a combustor is the burner where compressed air and fuel are mixed and then the mixture is combusted in the combustion chamber. The most common fuel for gas turbines is natural gas but also other gaseous fuels and liquid fuels are used in industrial gas turbines.

The object of this thesis is the burner which is used for SGT-800. This kind of gas turbine has 30 burners that is called “3rd generation Dry Low Emission” burner. See Figure 1.2



Figure 1.1 SGT - 800 3rd generation Dry Low Emission” burner

1.4 Computational Fluid Dynamics (CFD)

CFD, a branch of fluid dynamics, is applied as a cost-effective method of simulating real flows by the numerical solution of the governing equations. This branch of fluid dynamics provides cheaper means of testing fluid flow systems for complementing experimental and theoretical fluid dynamics. Also the conditions which are not possible or extremely difficult to measure experimentally and are not amenable to analytic solutions can allow to be investigated by this method.

In this thesis CFD simulations are performed by ANSYS CFX and FLUENT 13.0 software.

2 Theory

This chapter describes the basic theory which is used in this thesis. The most fundamental concept here is governing equations. The governing equations include the conservation of mass, momentum and energy of fluid element.

2.1 Conservation of mass

The law of conservation of mass states that for a closed system the amount of mass must be balanced and this amount remain constant throughout a process. In fluid dynamics expression, the net rate of mass flux which enters into a control volume is equal to the net rate of mass flux which flows out of the control volume. This can be defined by the equation below which is valid for any size of control volume.

$$\int_{CV} \frac{\partial \rho}{\partial t} dV = \sum_{in} \dot{m} - \sum_{out} \dot{m} \quad (2.1)$$

Figure 2.1 shows a fluid element with dimensions δx , δy and δz in Cartesian coordinate and the mass flux at all the six faces. The density ρ and three velocity components u in x -direction, v in y -direction and w in z -direction is considered at the center of the volume.

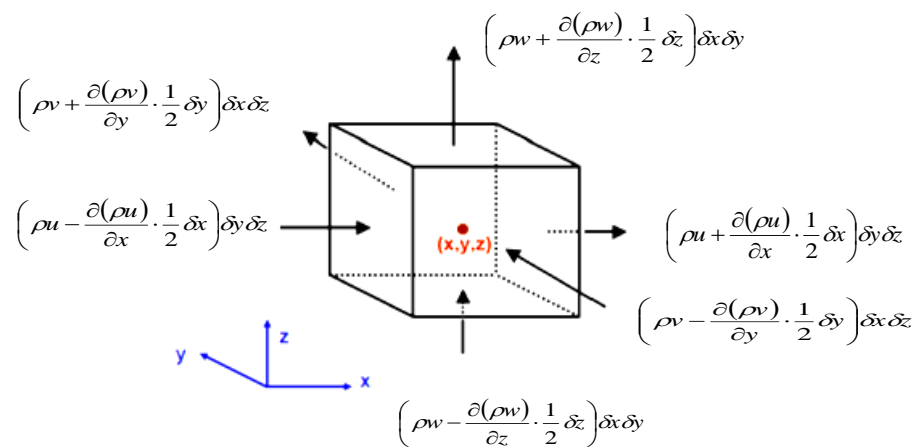


Figure 2.1 Fluid element with mass flux through the surfaces.

The equation of the mass conservation for this fluid volume for steady state condition can be written as

$$\begin{aligned}
& \left(\rho u - \frac{\partial(\rho u)}{\partial x} \cdot \frac{1}{2} \delta x \right) \delta y \delta z - \left(\rho u + \frac{\partial(\rho u)}{\partial x} \cdot \frac{1}{2} \delta x \right) \delta y \delta z \\
& + \left(\rho v - \frac{\partial(\rho v)}{\partial y} \cdot \frac{1}{2} \delta y \right) \delta x \delta z - \left(\rho v + \frac{\partial(\rho v)}{\partial y} \cdot \frac{1}{2} \delta y \right) \delta x \delta z \\
& + \left(\rho w - \frac{\partial(\rho w)}{\partial z} \cdot \frac{1}{2} \delta z \right) \delta x \delta y - \left(\rho w + \frac{\partial(\rho w)}{\partial z} \cdot \frac{1}{2} \delta z \right) \delta x \delta y = 0
\end{aligned} \tag{2.2}$$

Substituting these equation and then dividing by the fluid volume, $\delta V = \delta x \delta y \delta z$, the equation is obtained as

$$\frac{\partial(\rho u)}{\partial x} + \frac{\partial(\rho v)}{\partial y} + \frac{\partial(\rho w)}{\partial z} = 0 \tag{2.3}$$

For an adequately small control volume for transient flow equation (2.4) could be applied

$$\int_{cv} \frac{\partial \rho}{\partial t} dV \cong \frac{\partial \rho}{\partial t} \delta x \delta y \delta z \tag{2.4}$$

After combining equation (2.2) and (2.4) the complete continuity equation is given

$$\frac{\partial \rho}{\partial t} + \frac{\partial(\rho u)}{\partial x} + \frac{\partial(\rho v)}{\partial y} + \frac{\partial(\rho w)}{\partial z} = 0 \tag{2.5}$$

For incompressible fluids $\frac{\partial \rho}{\partial t} = 0$ so equation (2.5) can be rewritten as

$$\frac{\partial(\rho u)}{\partial x} + \frac{\partial(\rho v)}{\partial y} + \frac{\partial(\rho w)}{\partial z} = 0 \text{ or in more compact form } \nabla \cdot \bar{V} = 0 \tag{2.6}$$

2.2 Conservation of momentum

Conservation of momentum can be concluded from Newton's second law. According to Newton's second law change of momentum equals the sum of forces on a fluid particle. All forces can be calculated as mass times the acceleration, on a fluid element.

$$\bar{F}_{particle} = m_{particle} \bar{a}_{particle} \tag{2.7}$$

Acceleration is obtained as the derivative of the particle's velocity

$$\bar{a}_{particle} = \frac{d\bar{V}_{particle}}{dt} \tag{2.8}$$

At any moment the velocity of the particle equals the local velocity field at the particle's position. So

$$\bar{a}_{particle} = \frac{d\bar{V}_{particle}}{dt} = \frac{d\bar{V}(x_{particle}, y_{particle}, z_{particle}, t)}{dt} \tag{2.9}$$

$$= \frac{\partial \bar{V}}{\partial t} \frac{dt}{dt} + \frac{\partial \bar{V}}{\partial x_{particle}} \frac{dx_{particle}}{dt} + \frac{\partial \bar{V}}{\partial y_{particle}} \frac{dy_{particle}}{dt} + \frac{\partial \bar{V}}{\partial z_{particle}} \frac{dz_{particle}}{dt}$$

By considering $\frac{dx_{particle}}{dt}$, $\frac{dy_{particle}}{dt}$ and $\frac{dz_{particle}}{dt}$ same as velocity vector u , v and w respectively and also $(x_{particle}, y_{particle}, z_{particle})$ corresponds to the Eulerian form (x, y, z) , equation (2.9) can be rewritten as

$$\bar{a}(x, y, z, t) = \frac{d\bar{V}}{dt} = \frac{\partial \bar{V}}{\partial t} + u \frac{\partial \bar{V}}{\partial x} + v \frac{\partial \bar{V}}{\partial y} + w \frac{\partial \bar{V}}{\partial z} = \frac{\partial \bar{V}}{\partial t} + (\bar{V} \cdot \nabla) \bar{V} \quad (2.10)$$

Total derivative operator in equation (2.10) is also written as

$$\frac{D}{Dt} = \frac{d}{dt} = \frac{\partial}{\partial t} + (\bar{V} \cdot \nabla) \quad (2.11)$$

Now Newton's second law yields

$$\sum \bar{F} = m\bar{a} = m \frac{D\bar{V}}{Dt} = \rho dx dy dz \frac{D\bar{V}}{Dt} \quad (2.12)$$

The forces that act on a control volume in x-direction can be seen in *Figure 2.2*.

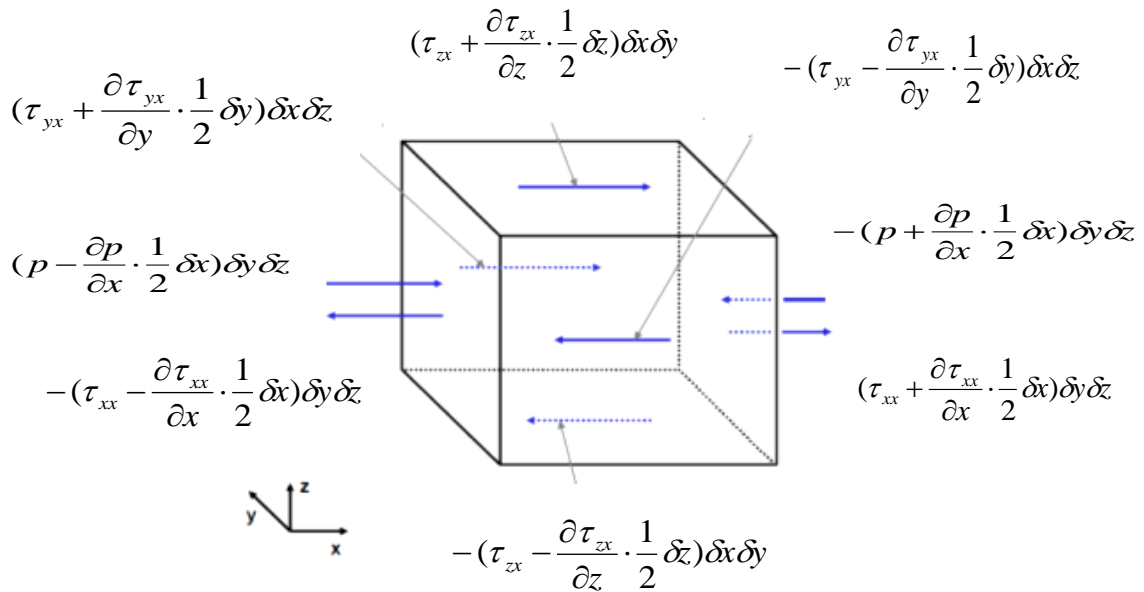


Figure 2.2 The forces in x-direction acting on each surface of the control volume

Net force in the x-direction is the sum of all the force components in that direction. The element body forces which act on the control volume in this direction are assumed as a single term S_x . So the momentum equation in x-direction can be written as

$$m \frac{Du}{Dt} = \left(\tau_{xx} + \frac{\partial \tau_{xx}}{\partial x} \cdot \frac{1}{2} \delta x \right) \delta y \delta z - \left(\tau_{xx} - \frac{\partial \tau_{xx}}{\partial x} \cdot \frac{1}{2} \delta x \right) \delta y \delta z$$

$$\begin{aligned}
& + (\tau_{yx} + \frac{\partial \tau_{yx}}{\partial y} \cdot \frac{1}{2} \delta y) \delta x \delta z - (\tau_{yx} - \frac{\partial \tau_{yx}}{\partial y} \cdot \frac{1}{2} \delta y) \delta x \delta z \\
& + (\tau_{zx} + \frac{\partial \tau_{zx}}{\partial z} \cdot \frac{1}{2} \delta z) \delta x \delta y - (\tau_{zx} - \frac{\partial \tau_{zx}}{\partial z} \cdot \frac{1}{2} \delta z) \delta x \delta y \\
& + (p - \frac{\partial p}{\partial x} \cdot \frac{1}{2} \delta x) \delta y \delta z - (p + \frac{\partial p}{\partial x} \cdot \frac{1}{2} \delta x) \delta y \delta z + S_x \delta x \delta y \delta z
\end{aligned} \tag{2.13}$$

By simplifying equation (2.13) and dividing by the element volume $\delta x \delta y \delta z$ obtains

$$\rho \frac{Du}{Dt} = \frac{\partial \tau_{xx}}{\partial x} + \frac{\partial \tau_{yx}}{\partial y} + \frac{\partial \tau_{zx}}{\partial z} - \frac{\partial p}{\partial x} + S_x \tag{2.14}$$

For the y-direction and z-direction the same equation could be derived in the same way, yielding

$$\rho \frac{Dv}{Dt} = \frac{\partial \tau_{xy}}{\partial x} + \frac{\partial \tau_{yy}}{\partial y} + \frac{\partial \tau_{zy}}{\partial z} - \frac{\partial p}{\partial y} + S_y \tag{2.15}$$

$$\rho \frac{Dw}{Dt} = \frac{\partial \tau_{xz}}{\partial x} + \frac{\partial \tau_{yz}}{\partial y} + \frac{\partial \tau_{zz}}{\partial z} - \frac{\partial p}{\partial z} + S_z \tag{2.16}$$

In more compact form, the three dimensional momentum equations are written as

$$\rho \frac{Du_i}{Dt} = \frac{\partial \tau_{ij}}{\partial x_j} - \frac{\partial p}{\partial x_i} + S_i \tag{2.17}$$

The viscous stress tensor τ_{ij} , requires modeling. According to the Newton's Law of Viscosity the viscous stress tensor for an isotropic fluid (viscosity is a scalar) is related to the first dynamic viscosity, μ for the linear deformations and the second viscosity, $\lambda = -2/3\mu$ for the volumetric deformations

$$\tau = \begin{bmatrix} \tau_{xx} & \tau_{xy} & \tau_{xz} \\ \tau_{yx} & \tau_{yy} & \tau_{yz} \\ \tau_{zx} & \tau_{zy} & \tau_{zz} \end{bmatrix} = \begin{bmatrix} 2\mu \frac{\partial u}{\partial x} + \lambda \text{div} \bar{V} & \mu (\frac{\partial u}{\partial y} + \frac{\partial v}{\partial x}) & \mu (\frac{\partial u}{\partial z} + \frac{\partial w}{\partial x}) \\ \mu (\frac{\partial u}{\partial y} + \frac{\partial v}{\partial x}) & 2\mu \frac{\partial v}{\partial y} + \lambda \text{div} \bar{V} & \mu (\frac{\partial v}{\partial z} + \frac{\partial w}{\partial y}) \\ \mu (\frac{\partial u}{\partial z} + \frac{\partial w}{\partial x}) & \mu (\frac{\partial v}{\partial z} + \frac{\partial w}{\partial y}) & 2\mu \frac{\partial w}{\partial z} + \lambda \text{div} \bar{V} \end{bmatrix} \tag{2.18}$$

For an incompressible flow $\text{div} \bar{V} = 0$ so if we consider an incompressible, isothermal Newtonian flow ($\rho = \text{constant}$, $\mu = \text{constant}$) we can end up to Navier-Stokes equation

$$\begin{aligned}
\text{x-momentum: } & \rho \left(\frac{\partial u}{\partial t} + u \frac{\partial u}{\partial x} + v \frac{\partial u}{\partial y} + w \frac{\partial u}{\partial z} \right) = - \frac{\partial p}{\partial x} + \mu \left(\frac{\partial^2 u}{\partial x^2} + \frac{\partial^2 u}{\partial y^2} + \frac{\partial^2 u}{\partial z^2} \right) + S_x \\
\text{y-momentum: } & \rho \left(\frac{\partial v}{\partial t} + u \frac{\partial v}{\partial x} + v \frac{\partial v}{\partial y} + w \frac{\partial v}{\partial z} \right) = - \frac{\partial p}{\partial y} + \mu \left(\frac{\partial^2 v}{\partial x^2} + \frac{\partial^2 v}{\partial y^2} + \frac{\partial^2 v}{\partial z^2} \right) + S_y
\end{aligned} \tag{2.19}$$

$$\text{z-momentum: } \rho \left(\frac{\partial w}{\partial t} + u \frac{\partial w}{\partial x} + v \frac{\partial w}{\partial y} + w \frac{\partial w}{\partial z} \right) = - \frac{\partial p}{\partial z} + \mu \left(\frac{\partial^2 w}{\partial x^2} + \frac{\partial^2 w}{\partial y^2} + \frac{\partial^2 w}{\partial z^2} \right) + S_z$$

2.3 Conservation of energy

According to the first law of thermodynamics energy can be neither created nor destroyed; it can only change in form. In other say the rate of energy change is equal to the rate of work done by the system plus the net heat transferred to the system. The total rate of change of energy is

$$\rho \frac{DE}{Dt} \quad (2.20)$$

Total rate of work done by the system can be calculated by multiplying the surface forces with velocity. These forces were shown in previous section. In *Figure 2.3* work done by surface forces in x-direction are illustrated.

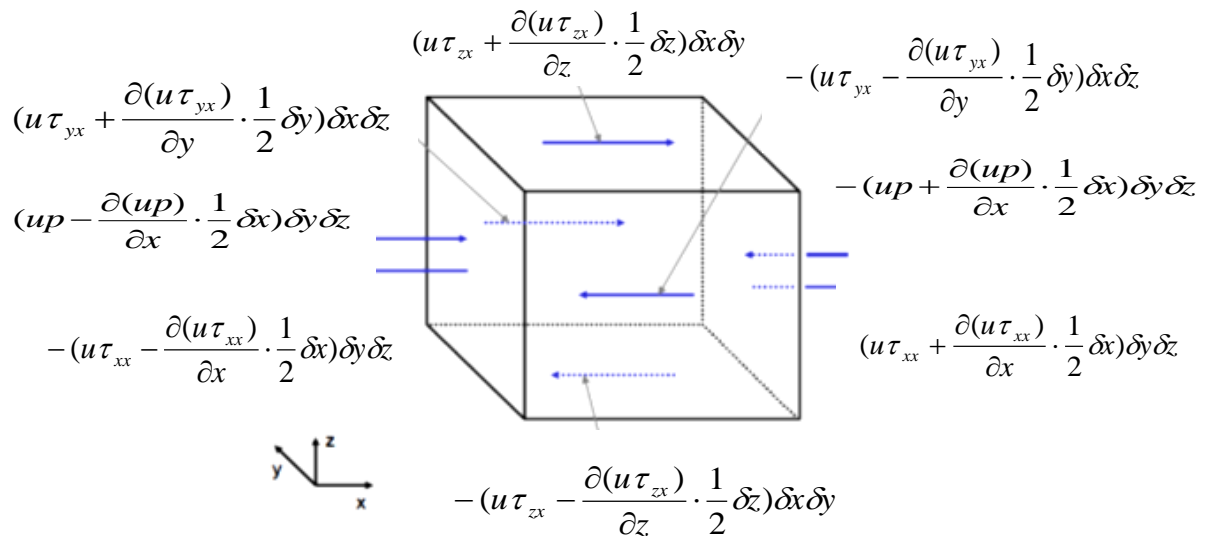


Figure 2.3 Work done by surface forces in x-direction

The work done in x-direction by the element can be written as

$$\begin{aligned} & \left(\tau_{xx} u + \frac{\partial \tau_{xx} u}{\partial x} \cdot \frac{1}{2} \delta x \right) \delta y \delta z - \left(\tau_{xx} u - \frac{\partial \tau_{xx} u}{\partial x} \cdot \frac{1}{2} \delta x \right) \delta y \delta z \\ & + \left(\tau_{yx} u + \frac{\partial \tau_{yx} u}{\partial y} \cdot \frac{1}{2} \delta y \right) \delta x \delta z - \left(\tau_{yx} u - \frac{\partial \tau_{yx} u}{\partial y} \cdot \frac{1}{2} \delta y \right) \delta x \delta z \\ & + \left(\tau_{zx} u + \frac{\partial \tau_{zx} u}{\partial z} \cdot \frac{1}{2} \delta z \right) \delta x \delta y - \left(\tau_{zx} u - \frac{\partial \tau_{zx} u}{\partial z} \cdot \frac{1}{2} \delta z \right) \delta x \delta y \\ & + \left(p u - \frac{\partial p u}{\partial x} \cdot \frac{1}{2} \delta x \right) \delta y \delta z - \left(p u + \frac{\partial p u}{\partial x} \cdot \frac{1}{2} \delta x \right) \delta y \delta z \end{aligned} \quad (2.21)$$

Add all terms and divide by the fluid element volume, $\delta x \delta y \delta z$, gives

$$\frac{\partial \tau_{xx} u}{\partial x} + \frac{\partial \tau_{yx} u}{\partial y} + \frac{\partial \tau_{zx} u}{\partial z} - \frac{\partial p u}{\partial x} \quad (2.22)$$

The same equation for y-direction and z-direction could be derived

$$\frac{\partial \tau_{xy} v}{\partial x} + \frac{\partial \tau_{yy} v}{\partial y} + \frac{\partial \tau_{zy} v}{\partial z} - \frac{\partial p v}{\partial y} \quad (2.23)$$

$$\frac{\partial \tau_{xz} w}{\partial x} + \frac{\partial \tau_{yz} w}{\partial y} + \frac{\partial \tau_{zz} w}{\partial z} - \frac{\partial p w}{\partial z} \quad (2.24)$$

In more compact form, the three dimensional momentum equations are written as

$$\frac{\partial \tau_{ji} u_i}{\partial x_j} - \frac{\partial p u_i}{\partial x_i} \quad (2.25)$$

The heat flux through each surface on a fluid element is shown in

Figure 2.3. The heat flux vector, q_i , describe the heat transferred to the system.

A heat flux balance can be written as

$$\begin{aligned} & (q_x - \frac{\partial q_x}{\partial x} \cdot \frac{1}{2} \delta x) \delta y \delta z - (q_x + \frac{\partial q_x}{\partial x} \cdot \frac{1}{2} \delta x) \delta y \delta z \\ & + (q_y - \frac{\partial q_y}{\partial y} \cdot \frac{1}{2} \delta y) \delta x \delta z - (q_y + \frac{\partial q_y}{\partial y} \cdot \frac{1}{2} \delta y) \delta x \delta z \\ & + (q_z - \frac{\partial q_z}{\partial z} \cdot \frac{1}{2} \delta z) \delta x \delta y - (q_z + \frac{\partial q_z}{\partial z} \cdot \frac{1}{2} \delta z) \delta x \delta y \end{aligned} \quad (2.26)$$

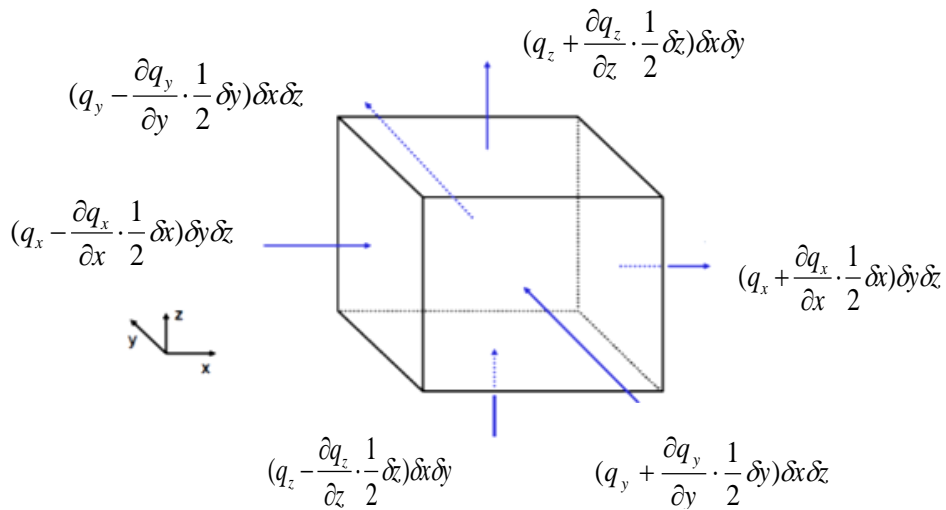


Figure 2.3 Surface heat flux in a fluid element

Again simplification and dividing by fluid element volume yields

$$-\frac{\partial q_x}{\partial x} - \frac{\partial q_y}{\partial y} - \frac{\partial q_z}{\partial z} \quad (2.27)$$

Corresponding to Fourier's law of heat conduction, for an isotropic fluid, the heat flux vector is related to temperature

$$q_x = -k \frac{\partial T}{\partial x} \quad (2.28)$$

Where k is the thermal conductivity;

By replacing q_x equation (2.27) can be rearranged as:

$$-\frac{\partial}{\partial x}(-k \frac{\partial T}{\partial x}) - \frac{\partial}{\partial y}(-k \frac{\partial T}{\partial y}) - \frac{\partial}{\partial z}(-k \frac{\partial T}{\partial z}) \quad (2.29)$$

According to first law of thermodynamics, the energy equation in three dimensions is

$$\rho \frac{DE}{Dt} = \frac{\partial \tau_{ji} u_i}{\partial x_j} - \frac{\partial p u_i}{\partial x_i} + \frac{\partial}{\partial x_i} (k \frac{\partial T}{\partial x_i}) + S_E \quad (2.30)$$

A source term S_E in equation (2.30) includes sources such as potential energy, sources due to heat production from chemical reactions, etc.

2.4 Scalar transport

The concentration of anything that does not affect the flow can be considered as scalar concentration. The rate of the concentration of a scalar in a cell is changed in two ways, convection and diffusion. The equation (2.31) expresses how the change of concentration of a scalar can be calculated.

$$\rho \frac{Dc}{Dt} = \Gamma \frac{\partial c}{\partial x_j} \quad (2.31)$$

In this equation c is the scalar concentration and Γ is the diffusion coefficient.

2.5 General transport equations

The various conservation equations have significant common parts. The conservative form of all fluid flow equations can usefully be written by a general variable ϕ . This equation is called general transport equation

$$\frac{\partial(\rho\phi)}{\partial t} + \text{div}(\rho\phi\bar{V}) = \text{div}(\Gamma \text{grad}\phi) + S_\phi \quad (2.32)$$

Or in words,

Rate of increase of ϕ of fluid element	+ Net rate of flow of ϕ out of fluid element (convection)	=	Rate of increase of ϕ due to diffusion	+ Rate of increase of ϕ due to sources
---	--	---	---	---

2.6 Reynolds average

For a fluctuating flow the values can be separated into a fluctuation part and a time averaged mean part. The equation in section 2.1 – 2.4 all have the instantaneous values of the variables. Hence each variable can be obtained by

$$\phi = \Phi + \phi' \quad (2.33)$$

The averaged value of any variable, Φ , of the instantaneous value of the variable, ϕ is calculated using the relation

$$\Phi = \frac{1}{\Delta t} \int_0^{\Delta t} \phi dt = \bar{\phi} \quad (2.34)$$

Ensemble averaging-equation 2-35- gives the same results as time averaging.

$$\Phi = \frac{1}{N} \sum_1^N \phi = \bar{\phi} \quad (2.35)$$

Corresponding to this, the momentum equation (2-19) can be written as

$$\rho \frac{D(U_i + u'_i)}{Dt} = -\frac{\partial(P + p')}{\partial x_i} + \mu \frac{\partial}{\partial x_j} \left(\frac{\partial(U_i + u'_i)}{\partial x_j} + \frac{\partial(U_j + u'_j)}{\partial x_i} \right) + S_i \quad (2.36)$$

Taking time average of the equation (2.35) leads to the Reynolds Averaged Navier Stokes (RANS)

$$\rho \frac{D(U_i)}{Dt} = -\frac{\partial P}{\partial x_i} + \mu \frac{\partial}{\partial x_j} \left(\frac{\partial U_i}{\partial x_j} \right) - \rho \frac{\partial \overline{u'_i u'_j}}{\partial x_j} + S_i \quad (2.37)$$

The noticeable difference is where the extra term $-\rho \frac{\partial \overline{u'_i u'_j}}{\partial x_j}$ appears. These terms

often behave such as stress terms and represent a correlation between the fluctuating velocities. These additional terms in general appear due to turbulence (fluctuating velocities) and are usually called Reynolds-stresses.

2.7 Closure problems

There are five governing equations in all; one equation for the conservation of mass, three equations for the conservation of momentum and one equation for the conservation of energy. But there are 17 unknowns in all; three unknown velocities, one unknown pressure, one unknown total energy, three unknown heat fluxes and nine unknown surface stresses.

The number of unknowns can be reduced to six with the assumption of Newtonian fluids and Fourier's law of heat conduction. Then the nine unknown surface stresses and three unknown heat fluxes are decreased to an unknown temperature and two fluid parameters. The system of equations is still impossible to solve and needs one more equation or one less unknown. By adding an equation of state for the fluid, e.g. the perfect gas law, the pressure is a function of density and temperature, the number of unknowns is reduced to five and the system of equations is closed as long as the necessary initial and boundary conditions are supplied.

However, according to section 2.6, there are more unknowns when Reynolds stresses appear. The number of these unknowns is six because the tensor is symmetric and total unknown would be eleven for a general case. This is called the closure problem: The number of unknowns is larger than the number of equations.

2.8 Turbulence

CFD calculations are more difficult in turbulent flow, which is almost always the case, than in a laminar case. Turbulence occurs when the convective forces of the flow are much larger than viscous forces, causing three-dimensional, rapid, unsteady and nonlinear so called eddies. The time- and length scale of these eddies can change in several orders of magnitude and that could be in all directions of the flow. The strength of the turbulence may be estimated using the Reynolds number, which is the ratio of convective to viscous forces. Turbulence calculation in CFD is performed in a few ways such as:

DNS: In the direct numerical simulation (DNS) method, the motions for all scales of the turbulence are solved. Therefore a DNS simulation depends highly on an extremely fine grid and this requires extremely powerful computers. Because of that the DNS hardly is useful when simulating even for the simplest flow. Also when the Reynolds number is high the turbulence in the flow increases which makes it even harder.

LES: In large eddy simulation (LES) only the motion for the larger eddies in the flow are resolved and the smaller scale eddies are modeled. In this method the smaller eddies are assumed to be isotropic i.e. they are assumed to behave in a statistically predictable way regardless of the turbulent flow field. The LES demands much less computer resources compared to DNS but still the requirement is considerable.

The most practical way so far has been modeling all the turbulent eddies with a specific turbulence model. In this case none of eddies, not even the largest ones are resolved but instead the features of turbulence like enhanced mixing and diffusion is modeled. Applying such a turbulence model means the Navier-Stokes equation is replaced by a Reynolds-averaged Navier-Stokes equation (RANS).

2.9 Turbulence models

Turbulence models are generally categorized corresponding to the governing equations they apply to (e.g. Reynolds-averaged Navier-Stokes or Large Eddy Simulation equations). This thesis work is based on Reynolds-averaged Navier-Stokes (RANS) equations in steady state situations so the discussion is limited to models for the Reynolds-averaged Navier-Stokes (RANS) equations here.

2.9.1 Algebraic (Zero-Equation) Models

Algebraic models are the simplest models. An algebraic equation is applied to compute a turbulent viscosity, often called “eddy” viscosity. This model does not solve an additional transport equation in order to predict the contributions of the turbulence and because of that these are called “zero-equation” models. The Reynolds

stress tensor is calculated by applying Boussinesq assumption. This assumption relates Reynolds stress tensor to the velocity gradients and the turbulent viscosity.

$$\overline{\rho u_i u_j} = -\mu_t \left(\frac{\partial U_i}{\partial x_j} + \frac{\partial U_j}{\partial x_i} \right) + \frac{2}{3} \rho k \delta_{ij} \quad (2.38)$$

$k = \frac{1}{2}(u'^2 + v'^2 + w'^2)$ is the turbulence kinetic energy. μ_t is related to the eddy viscosity and is a property of the flow, not the fluid. μ_t can be computed as

$$\mu_t = C \rho \ell \mathcal{G} \quad (2.39)$$

Where C is a proportionality constant, ℓ is a turbulence length scale and \mathcal{G} is a turbulent velocity scale. Hence a model for k , ℓ and \mathcal{G} is required to close the system.

2.9.2 One-Equation Models

In these models a single transport equation is solved for a turbulent quantity (usually the turbulent kinetic energy) and a second turbulent quantity (usually a turbulence length scale) is calculated from an algebraic expression. Boussinesq assumption is used to calculate the turbulent viscosity.

$$\mu_t = \rho \ell \sqrt{k} \quad (2.40)$$

The dissipation of kinetic energy is assumed to be related to the kinetic energy as

$$\varepsilon = \frac{C_D k^{3/2}}{\ell} \quad (2.41)$$

Where C_D is a constant.

2.9.3 Two-Equation Models

As their name states, these models need the solution of two additional governing equations in order to compute the contributions of turbulence to the mean flow. The most common transported variables are the turbulent kinetic energy and the turbulent dissipation (k-epsilon) or the turbulent specific dissipation (k-omega). The second variable can be considered as the variable that specifies the length- or time scale of the turbulence.

There are many models (too numerous to mention) but two of the most common models are the SST model and the k-epsilon model.

The Shear-Stress transport model (SST) is a combination of a k-omega model, which is utilized near walls, and a k-epsilon model, which is utilized in regions far from walls. This model is reasonably robust and does in general a good job near solid boundaries. [ANSYS (2010)]

The k-epsilon model is a model based on transport equations for the turbulence kinetic energy (k) and its dissipation rate (ε). The model that is used in this thesis is k-epsilon model so just this model is explained here. The eddy viscosity is assumed to be related with the kinetic energy as

$$\mu_t = C_\mu \rho \frac{k^2}{\varepsilon} \quad (2.42)$$

Where C_μ is a model constant.

The values for the kinetic energy and the eddy dissipation are obtained directly from their differential transport equation

$$\rho \frac{Dk}{Dt} = \nabla \cdot \left[\left(\mu + \frac{\mu_t}{\sigma_k} \right) \nabla k \right] + P_k - \rho \varepsilon \quad (2.43)$$

$$\rho \frac{D\varepsilon}{Dt} = \nabla \cdot \left[\left(\mu + \frac{\mu_t}{\sigma_\varepsilon} \right) \nabla \varepsilon \right] + \frac{\varepsilon}{k} (C_{\varepsilon 1} P_k - C_{\varepsilon 2} \rho \varepsilon) \quad (2.44)$$

Where $C_{\varepsilon 1}, C_{\varepsilon 2}, \sigma_k$ and σ_ε are constants and P_k is the turbulence production due to viscous and buoyancy forces and modeled as

$$P_k = \mu_t \nabla \bar{V} \cdot (\nabla \bar{V} + \nabla \bar{V}^T) - \frac{2}{3} \nabla \cdot \bar{V} (3\mu_t \nabla \cdot \bar{V} + \rho k) + P_{kb} \quad (2.45)$$

Where P_{kb} is the buoyancy production term. [Larsson E. (2009), <http://www.innovative-cfd.com/turbulence-model.html>]

2.10 Law of the wall

Turbulent flows are considerably affected by presence of walls. Viscous damping reduces the tangential velocity fluctuations in regions very close to the wall, while kinematic blocking reduces the normal fluctuations. However the turbulence is rapidly enlarged by the production of turbulence kinetic energy due to large gradients in mean velocity, toward the outer part of the near wall region.

In fluid dynamics the average velocity of a turbulent flow at a certain point is proportional to the logarithm of the distance from that point to the wall or the boundary of fluid region.

Various experiments have shown that the near wall region can be mainly subdivided by three layers; “viscous sub layer” which is the innermost layer where the flow is almost laminar and the molecular viscosity have an important role in momentum and heat or mass transfer. The outer layer is called the fully-turbulent layer and turbulence has a major role. The region between the viscose sub layer and fully turbulent is an interim region where the effect of molecular viscosity and turbulence are equally important. Figure 2.5 illustrate the law of he wall.

The logarithmic law of the wall is valid for flows over flat surfaces and at high Reynolds numbers and a solution for the mean velocity parallel to the wall is estimated by

$$u^+ = \frac{1}{k} \ln y^+ + C^+ \quad (2.46)$$

$$y^+ = \frac{yu_\tau}{\nu} \quad , \quad u_\tau = \sqrt{\frac{\tau_w}{\rho}} \quad \text{and} \quad u^+ = \frac{u}{u_\tau} \quad (2.47)$$

Where:

y^+ : is the distance from the wall measured in friction velocity u_τ and kinematic viscosity ν

u^+ : is the dimensionless velocity

τ_w : is the wall shear stress

u_τ : is called the friction velocity or shear velocity

κ : is the Von Kármán constant

C^+ : is a constant

From experiments, the Von Kármán constant is found to be $\kappa \approx 0.41$ and $C^+ \approx 5.0$ for a smooth wall.

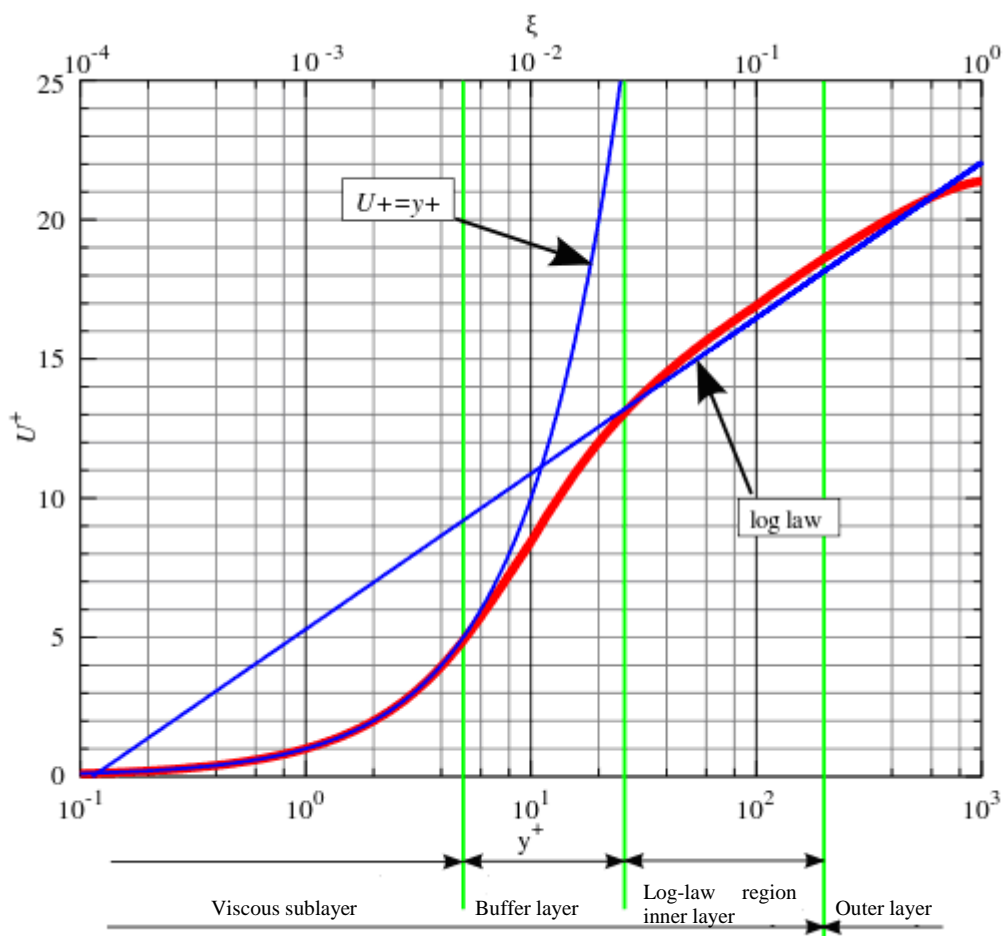


Figure 2.5 Law of the wall, horizontal velocity near the wall with mixing length model

2.10.1 Near the wall

There are other estimations for friction velocity for viscous Sub layer and buffer layer.

In the region of the viscous sub layer (less than 5 wall units) the variation of u^+ to y^+ is more or less 1:1, it can be written as

$$\text{For } y^+ < 5 \rightarrow u^+ = y^+ \quad (2.48)$$

This estimation can be used farther than 5 wall units, but by $y^+ = 12$ the error is more than 25%. In the region known as buffer layer, between 5 wall units and 30 wall units, neither law holds, such that

$$\text{For } 5 < y^+ < 30 \rightarrow u^+ \neq y^+ \quad \text{and} \quad u^+ \neq \frac{1}{k} \ln y^+ + C^+ \quad (2.49)$$

3 Methodology and results

This chapter is used to explain the project procedures and show how turbulent mixing in a jet in cross flow (JIC) is simulated.

The purpose of this project is to obtain an optimized mesh strategy for simulating a jet in cross flow related to a SGT-700/800 burner. At the first step, the behavior of fluid flow for turbulent mixing in a jet in cross flow is investigated. The equations have been solved by two soft wares; ANSYS CFX and Fluent 13.0 and the results are compared with a reference case.

The fuel-air mixing and radial profile at the burner outlet has been shown in previous work to not fulfill the grid independence requirements.

3.1 SGT-700/800 burner

The SGT- 700/800 burners are 3rd generation Dry Low Emission burners. Each burner has up to 40 nozzles in the swirler part. The swirler is created by 4 quatro-cones which are shifted slightly in order to allow the air to enter the swirler. Up to 9 nozzles are placed in each slot and the remaining 4 nozzles are located in the space cap. Figure 3.1 illustrates the burner.

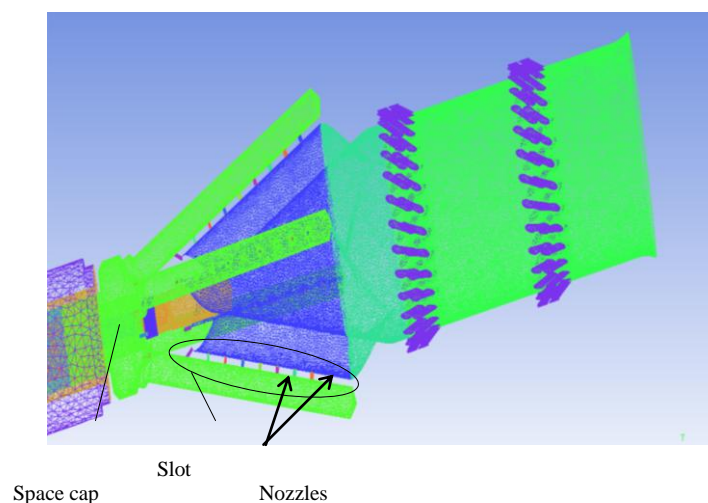


Figure 3.1 SGT-800 burner

In the SIT (Siemens Industrial Turbomachinery) mesh that is provided for the SGT-800 burner, the refined regions are supposed to cover the jet trajectories. But following the jet trajectory in the burner is not easy, because the nozzles are close to each other so the fluid flow of each jet is affected by the adjacent nozzles and also the swirling flow makes the jet trajectory complicated to predict beforehand.

Refined regions in the SIT strategy are considered along each nozzle axis, in one third of the channel width but there are also refinement regions in the direction of the nozzle row downstream the nozzles. The density boxes in the direction of the nozzle row are arranged in a way that covers the jet trajectory. As is shown in *Figure 3.1* there are 3 density boxes which include all jets down stream. However this type of

downstream refinement creates the same cell size in the jet trajectory as in between them, which might not be optimum due to unnecessary cells.

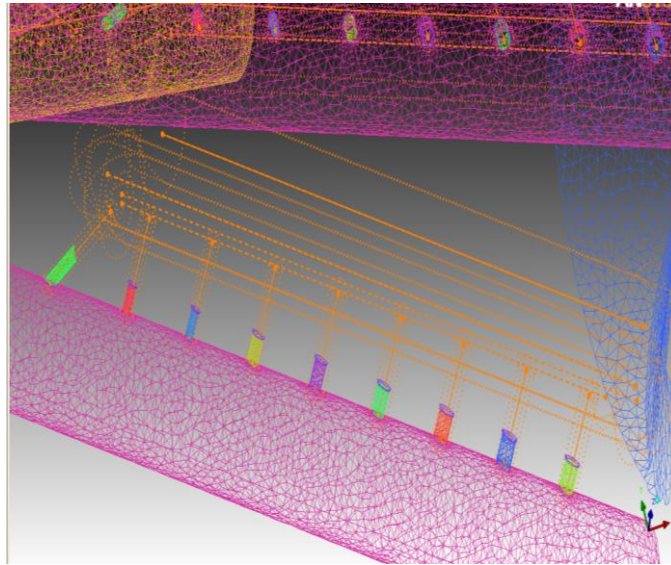


Figure 3.1 density boxes SIT strategy

3.2 Reference case

All the results in this project have been compared to the reference case results. The reference case is the study entitled “Mixing Studies Quantitative determination of the turbulent fuel/air mixing at gas turbine relevant conditions” and was done in the Combustion Technology division of Engler-Bunte institute, Karlsruhe University and Siemens in Mulheim, Germany and Orlando, USA. [Galeazzo F., Donnert G., Habisreuther P., Zarzalis N., Valdes R., Krebs W. (2010)]

In this study the JIC configuration under engine relevant condition had been investigated both numerically and experimentally.

3.2.1 Domain

The numerical domain in this case is a planar channel for the cross flow and a long pipe which is used to feed the jet. The domain is shown in *Figure 3.2*.

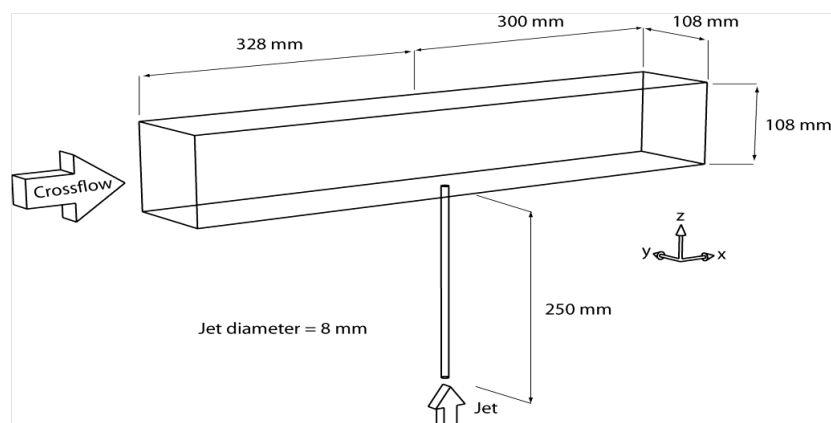


Figure 3.2 Overview of reference case with dimensions

3.2.2 Grid

The grid in the reference case had approximately 6 million elements and 1.4 million nodes. The numerical grid was composed of 5 layers prism elements at the walls and tetrahedral elements in the core with element sizes equivalent to $1/20D$. Also there are refinement regions that follow the jet trajectory. See Figure 3.4.

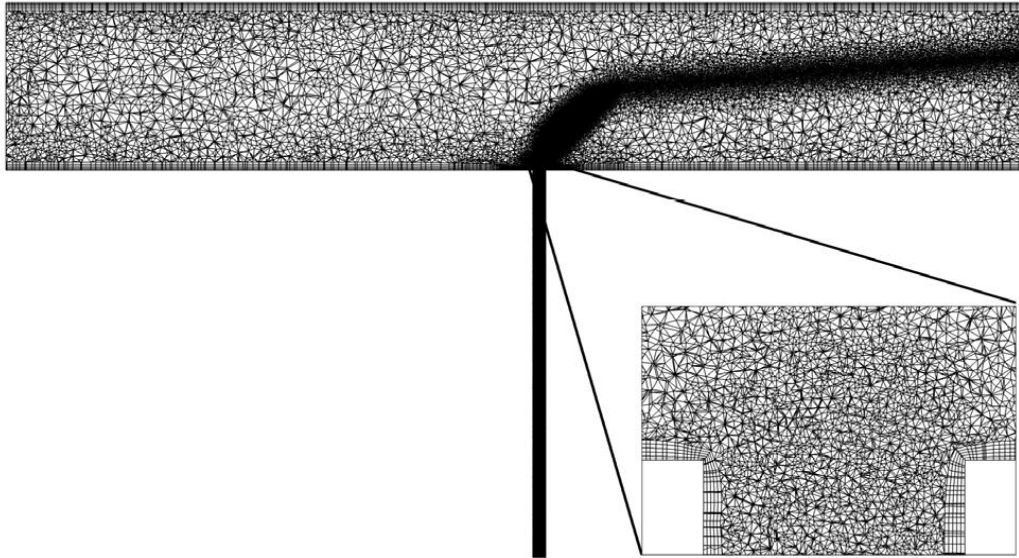


Figure 3.4 Numerical grid on symmetry plane, reference case

Table 3.1 Reference case grid specification

Grid specification for SIT case	
Number of cells	6,000,000
Mesh Type	Tetrahedral
Element size	
Refined region	$1/20D$
Other region	$1/8 D$
Pipe wall region	$1/20 D$
Structure type	Unstructured
Blocking	$\approx 0.3 \%$
Prism	5 layers
Orthogonal quality	≥ 0.23

3.2.3 Boundary conditions

All cases in this project have the same boundary condition as the reference case. The main parameter which describes a jet in cross flow is the jet-to-cross flow velocity ratio, R . This is calculated as the square root of the momentum ratio: $R = (\rho_{jet} U_{jet}^2 / \rho_{cross} U_{cross}^2)^{1/2}$, where U_{jet} is the bulk jet velocity and U_{cross} is the maximum cross flow velocity in a plane $1.5 D$ upstream of the jet inlet. In this experiment the jet density and cross flow density have been considered equal ($\rho_{jet} = \rho_{cross}$) so the velocity ratio can be expressed as $R = U_{jet} / U_{cross}$. The experimental condition which is given in Table 3.2 using $R=4$.

Table 3.2 Boundary conditions

Cross flow Inlet	Bulk velocity	9.08 m/s
	U_{cross}	9.43 m/s
	Turbulence intensity	1.5%
	Re	6.24×10^4
Tube Inlet	Bulk velocity	37.72 m/s
	Turbulence intensity	5%
	Re	1.92×10^4

For the mixing of two flows a passive scalar has been used as a tracer. The value of this dimensionless scalar concentration has been set to 1 into the pure pipe flow and 0 into the pure cross flow.

3.2.4 Experimental Set-up

The experiment used the boundary conditions with cross flow Reynolds number set at 6.24×10^4 and the jet flow Reynolds number at 1.92×10^4 . The experimental model is exactly similar the domain that is shown in Figure 3.3. The measurement techniques that were used for this experiment are PIV (Particle Image Velocimetry) for the velocity and LIF (Laser Induced Fluorescence) for concentration. The air with aerosol particles (DEHS, diameter $< 2 \mu m$) is used for PIV measurements while for LIF measurement 5000 ppm of NO_2 were added to the jet flow.

3.3 Turbulence modeling

The turbulence model which is applied here is a RANS turbulence model, k-epsilon. K-epsilon is known as the industry standard model and has been applied in most general purpose CFD codes.

Within ANSYS CFX, the k-epsilon turbulence model uses the scalable wall-function approach to resolve the near wall flow features. [ANSYS (2010)]

Within Fluent, the realizable k-epsilon model has been used and the approach to resolve the near wall flow features is chosen as the standard wall function. [ANSYS (2010)]

3.4 Solvers and models:

The cases have been investigated in steady state mode. In Fluent for the first iterations the spatial discretization is set as first order scheme and standard k-epsilon is chosen and then second order scheme together with the realizable k-epsilon model.

In the simulations it is assumed isothermal condition. Air at 298 K, density equals to 1.185 kg.m^{-3} and dynamic viscosity equals to $1.831 \times 10^{-5} \text{ kg.m}^{-1}.\text{s}^{-1}$, has been selected as material in the whole domain for both cross flow and jet. For the mixing of two flows a passive scalar has been used as a tracer in CFX and user defined Scalar in Fluent. The value of this dimensionless scalar concentration has been set at 1 at the pipe flow inlet and 0 at the cross flow inlet. [Galeazzo F., Donnert G., Habisreuther P., Zarzalis N., Valdes R., Krebs W. (2010)]

3.5 Parameter study

The parameters which are studied in this thesis are mostly velocity magnitude, velocity in x direction (u) and the dimensionless concentration C.

The dimensionless concentration C, is modeled as a passive scalar (tracer in CFX and user defined scalar in Fluent) for the mixing of the two flows. Figures below illustrate the velocity contour and C contour for the reference case.

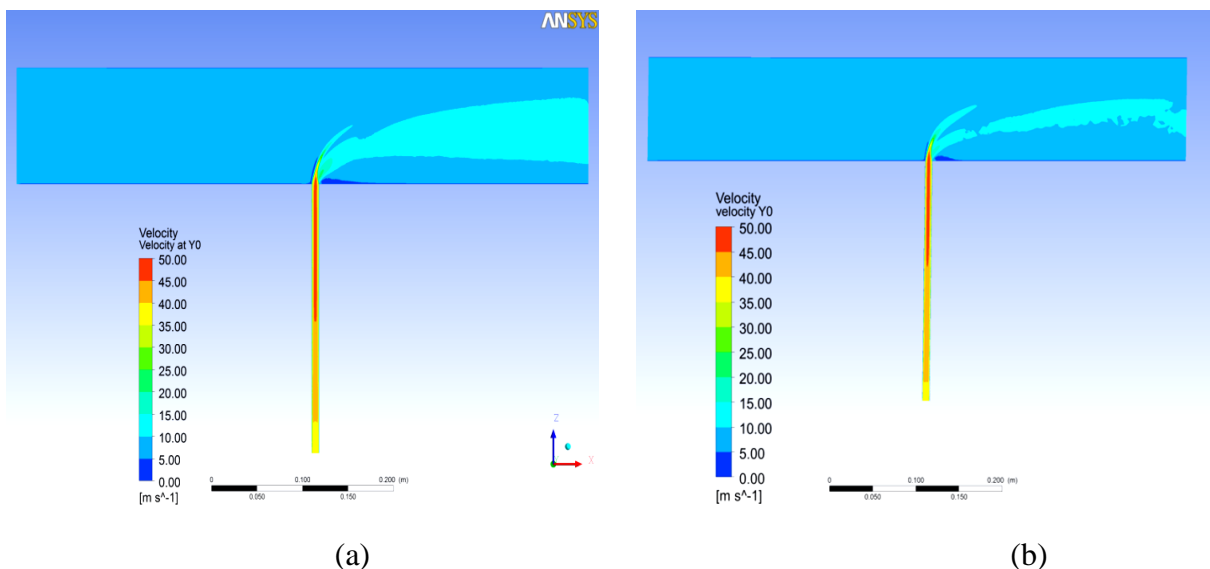


Figure 3.5 velocity contour in symmetry plane, Reference case, (a) CFX; (b) Fluent

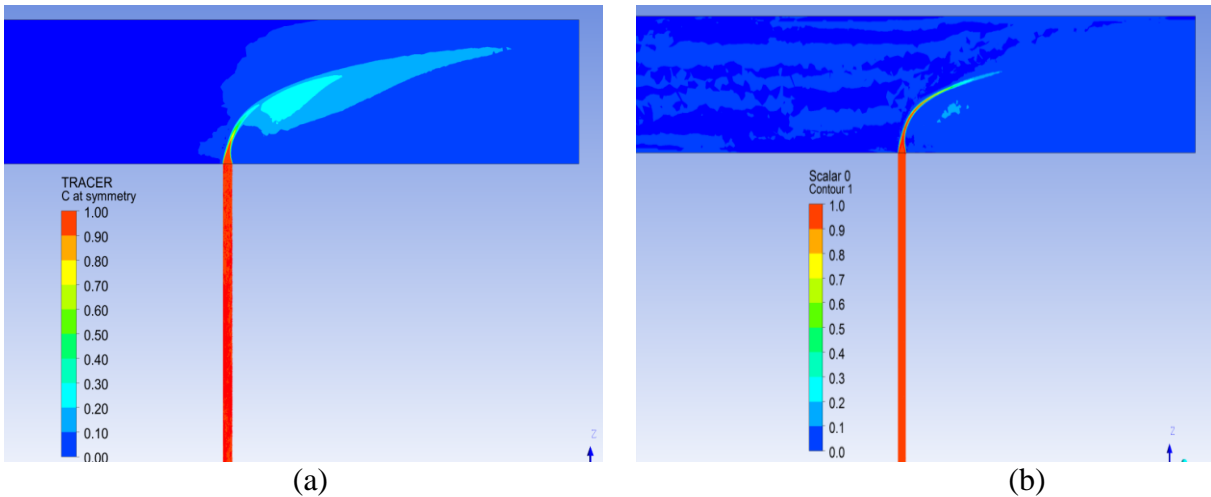


Figure 3.6 C at symmetry Plane, reference case, (a) CFX; (b) Fluent

The results for the velocity component in x direction (u) and z direction (w) for CFX and Fluent are shown in Figure 3.7. The data are taken 1D downstream ($X/D=1$) of the pipe center and varying 0-6 D along the z -direction. As can be seen the CFX and Fluent results don't match. Therefore, since the goal is to find a grid independence solution, Fluent is selected as the main tool due to the grid adaption capability. Later on in this thesis the differences between Fluent and CFX are addressed again. The CFX results can be found in the appendix.

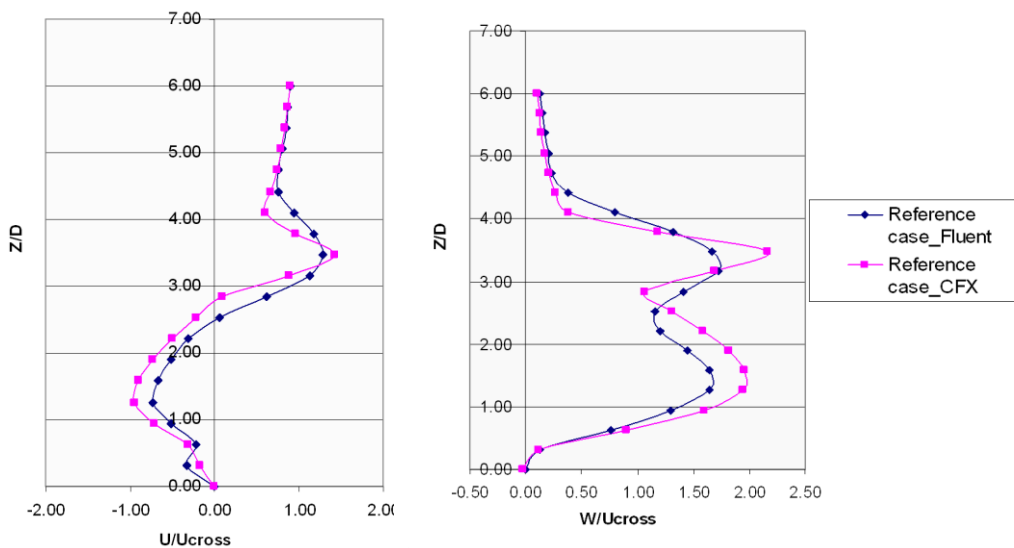


Figure 3.7 Profiles of velocity components U/U_{cross} and W/U_{cross} 1D downstream, $x/D=1$, $y=0$, CFX and Fluent results

3.6 SIT case

As mentioned earlier the computational domain in all investigated cases in this thesis is the same as the reference case but to save computation time a symmetry plane was introduced reducing the domain to half.

The mesh strategy usually used for the SGT-800 burner is applied for the SIT case.

3.6.1 Mesh Generation

The program that has been used for mesh generation is ICEM. Since the preparation of structured grid is very time consuming, unstructured grid with tetrahedral cells has been generated mostly.

The most efficient method of TET-mesh generation is to first build a surface mesh and then use the quick Delaunay algorithm to mesh the volume. For the surface mesh the patch independent method has been used. When the surface mesh is completed the mesh has to be checked and any errors and problems have to be fixed. In the next step the mesh has to be smoothed to achieve the proper mesh quality since low quality of the mesh can affect the results.

After smoothing the surface mesh, by utilizing the Delaunay algorithm the volume is generated. As for the surface mesh the volume mesh has to be checked for possible errors and then smoothed furthermore.

In this thesis it has been attempted to create the surface mesh with a quality of 0.3 and above. The minimum quality for the volume mesh has been attempted to keep above 0.3 for most cases but for some around 0.2 was achieved which is sufficient enough.

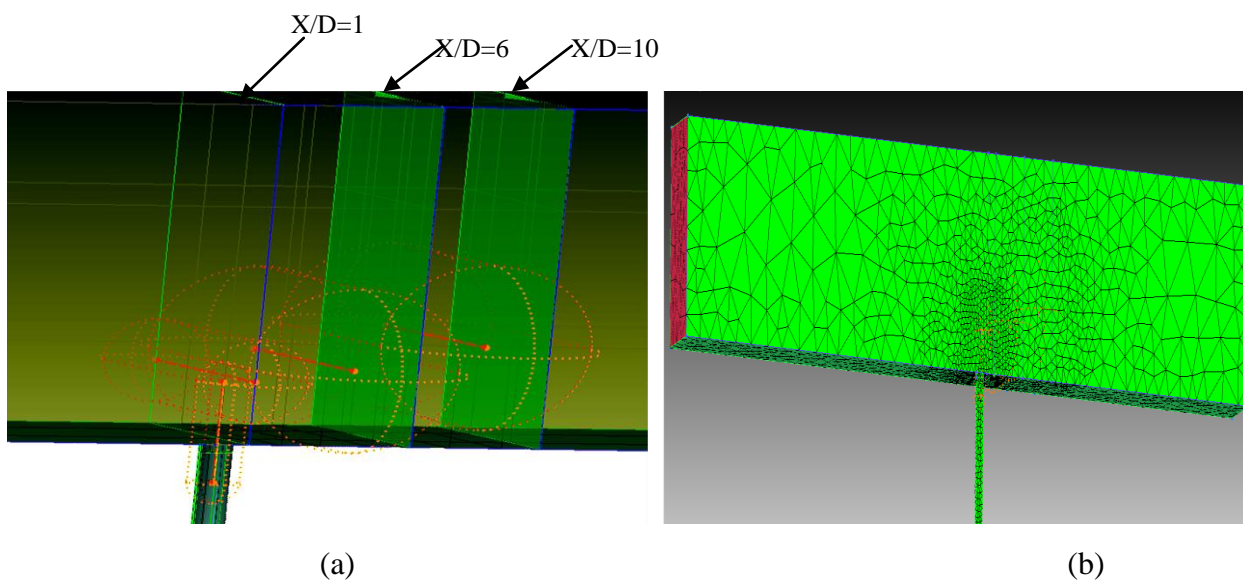


Figure 3.8 (a) SIT case density boxes, (b) SIT case mesh

The density boxes for the SIT mesh are organized in a similar way as for the SGT-800 burner, as is shown in Figure 3.8. One cylindrical density box is placed along the nozzle axis, in a way that covers the pipe nozzle from $Z/D = -1.5$ and to $Z/D = 2.5$ into the channel region. The cell size of this density box is around $0.4D$. The next three density boxes are cylindrical density boxes where their center lines are along the y -direction. The nearest one is located at $x=0.008$ and $z=0.020$ with cell size around $0.4D$. The next two ones are located at $x=32$, $Z=24$ and $x=64$, $z=32$ with cell size $0.8D$.

As can be seen in Table 3.3 and Figure 3.8 the grid resolution with the SIT strategy is much lower as compared to the reference case. The results for both simulations need to be investigated in order to understand how and in which region the SIT case should be improved and optimized.

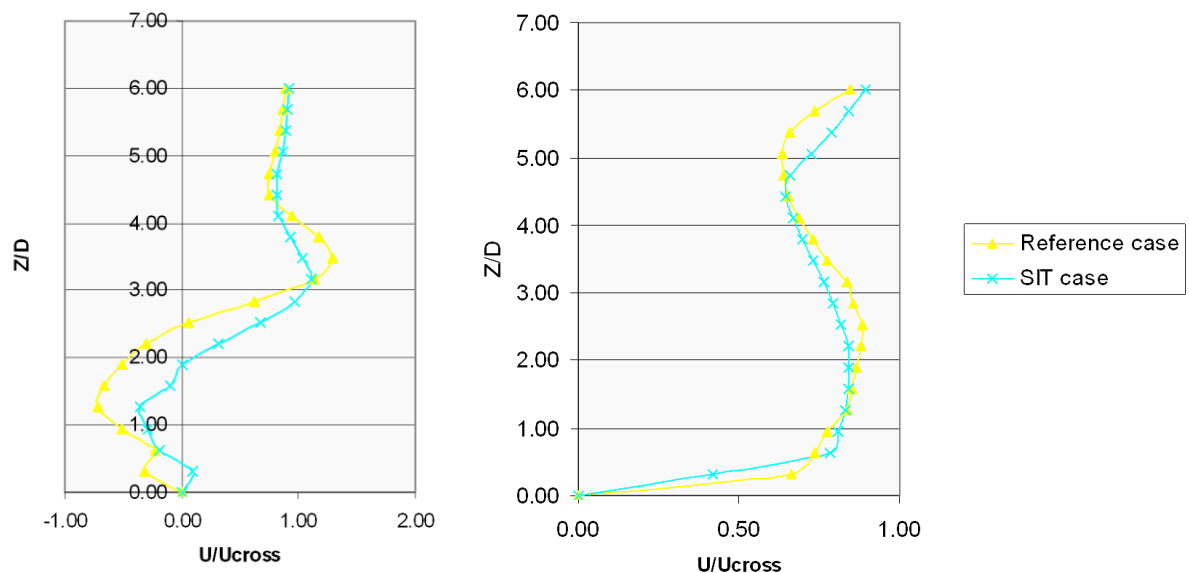
The grid specification for the SIT case is shown in Table 3.3.

Table 3.3 SIT case grid specification

Grid specification for SIT case	
Number of cells	48,972
Mesh Type	Tetrahedral
Element size	
Refined region	0.4D-0.8D
Other region	1.6 D
Pipe wall region	0.2 D
Structure type	12 Aligned nodes per 360°
Blocking	≈ 5%
Prism	No prism
Orthogonal quality	≥0.53

3.6.2 Results:

The profile of the velocity component U at the symmetry plane ($y=0$) at $X/D=1, 6, 10$ and at the outlet, are compared to the reference case. As can be seen in Figure 3.9 there is significant difference between the grids.



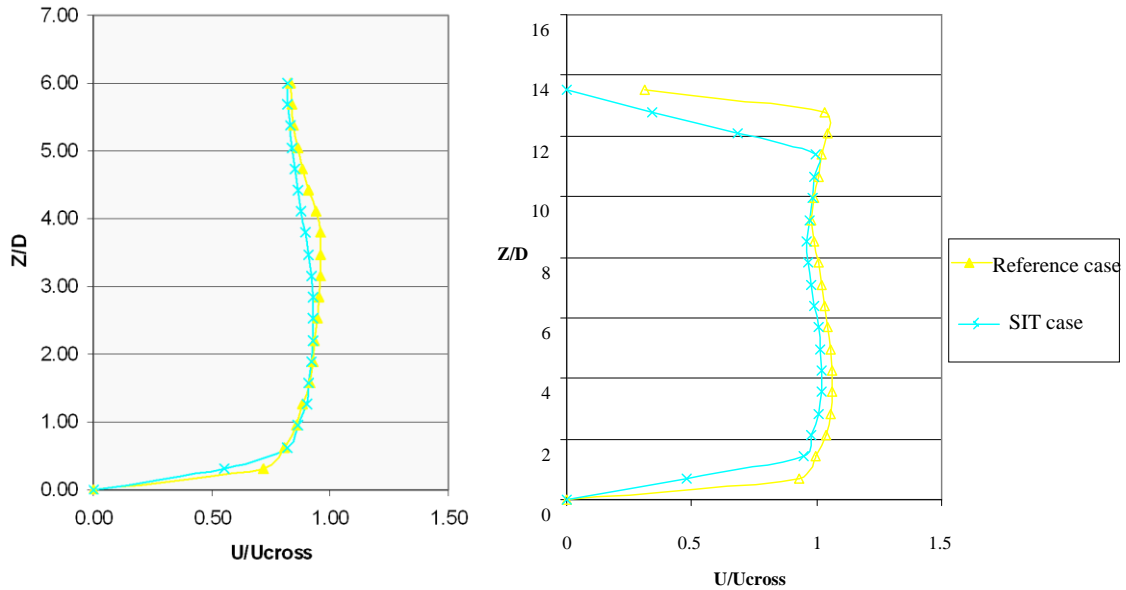


Figure 3.9 Profiles of velocity components U/U_{cross} at $X/D=1,6,10$ and outlet, Reference case vs. SIT using Fluent

According to the above figure, the grid resolution should be improved. Refined region should be selected carefully to avoid unnecessary increase in number of cells. Considering density boxes along the jet trajectory should be a good choice.

3.7 Case study I: density boxes along jet trajectory

3.7.1 Mesh generation

The mesh has been created in a similar way as the SIT case. As compared to the SIT strategy, the only difference is unstructured grid in the pipe nozzle and different density boxes.

In this case four density boxes with the same cell size of $1/4 D$ are used along the jet trajectory until $X/D=10$. The grid is illustrated in Figure 3.10 and the grid specification is shown in Table 3.4.

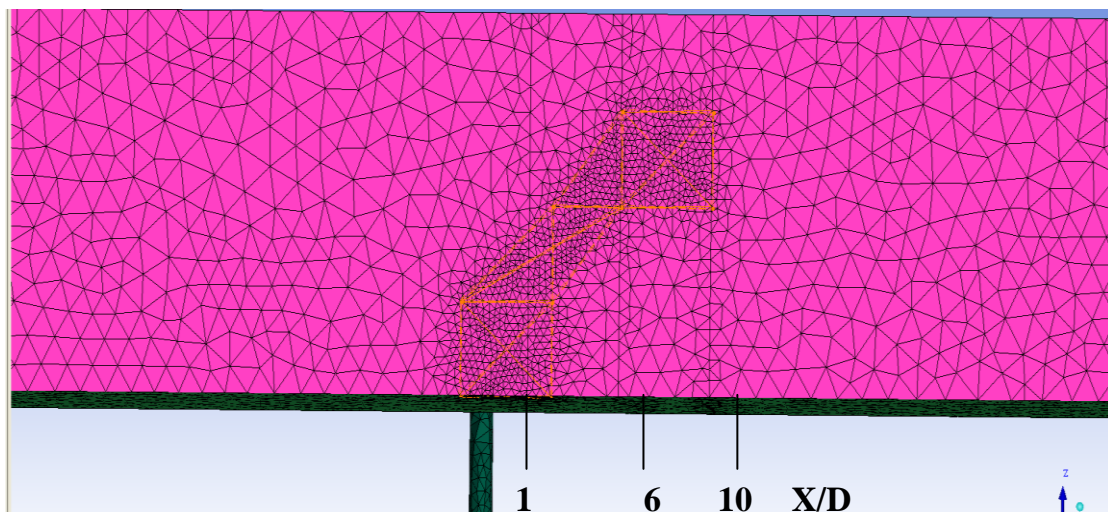


Figure 3.10 case Study I grid

Table 3.4: Case study I grid specification

Grid specification for case I	
Number of cells	108,256
Mesh Type	Tetrahedral
Element size	
Refined region	1/4D
Other region	1 D
Pipe wall region	1/2 D
Structure type	Unstructured
Blocking	≈ 5-10%
Prism	No prism
Orthogonal quality	≥0.48

3.8 Case study II: structured grid in nozzle pipe

In this section the effect of unstructured grid in nozzle pipe are investigated.

3.8.1 Blocking effect

Unstructured grid in the jet pipe leads to nozzle blocking and may have a great effect on the accuracy. Proper structured grid can improve the grid resolution and is easy to implement. The circular segment (green area) in Figure 3.11 is the blocked area in the structured grid and can be calculated as:

$$A_s = \pi \times R^2 - N \times \frac{R^2 \sin \theta}{2}$$

$$\text{Blocking \%} = \frac{A_s}{A} = 1 - \frac{N}{2\pi} \sin \theta$$

Where:

A_s = Circular segment area

A = hole area

$\theta = 2\pi/N$ where N is the number of tangential aligned cells for a 360° hole

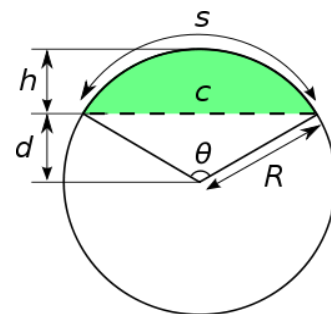


Figure 3.11: a circular segment

The blocking percentage is calculated for some values of N in Table 3.5:

Table 3.5: Blocking percent

Number of tangential aligned cells for a 360° hole (N)	Blocking
8	9.97%
12	4.51%
16	2.55%
24	1.14%
32	0.64%
48	0.29%
64	0.16%

3.8.2 Aligned nodes cases

The investigated cases here have similar refined regions as case study I but there are aligned nodes around the pipe wall. The study is done for N= 16, 32 and 64.

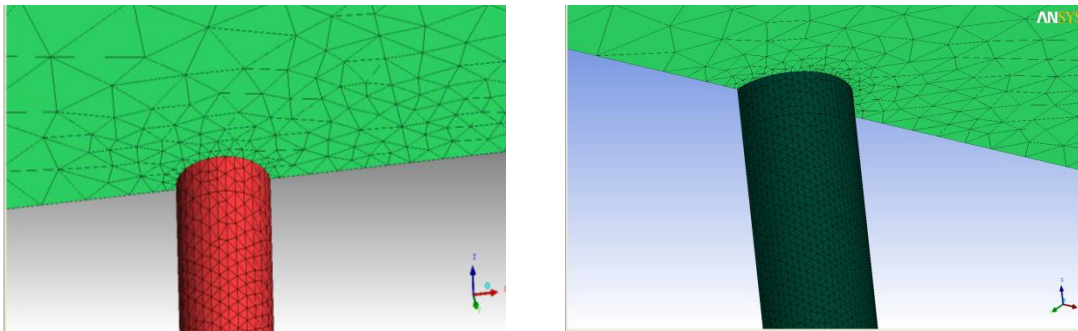


Figure 3.12 Structured wall pipe a) 32, b) 64 aligned nodes

Table 3.6 Case study II grid specification

	Dens1_aligned node 16	Dens1_aligned node 32
Number of cells	160,116	340,735
Mesh Type	Tetrahedral	Tetrahedral
Element size		
Refined region	1/2D	1/2D
Other region	1 D	1 D
Pipe wall region	1/16 D	1/32 D
Structure type	16 Aligned nodes per 180°	32 Aligned nodes per 180°
Blocking	0.6%	0.16%
Prism	No prism	No prism
Orthogonal quality	≥ 0.5	≥ 0.5

3.8.3 Results

The results for the different grid in Table 3.4 and 3.6 as compared to reference case are shown in Figure 3.13.

The outcomes for the case with 8 aligned nodes around the half pipe are improved compared to the unstructured grid but still don't match with the reference results. Using 16 and 32 aligned nodes around half jet pipe improved pipe wall resolution greatly and consequently the results improved noticeably, see the profile of velocity component U, at symmetry plane ($y=0$) in $X/D=1, 6$ and 10 in figure below.

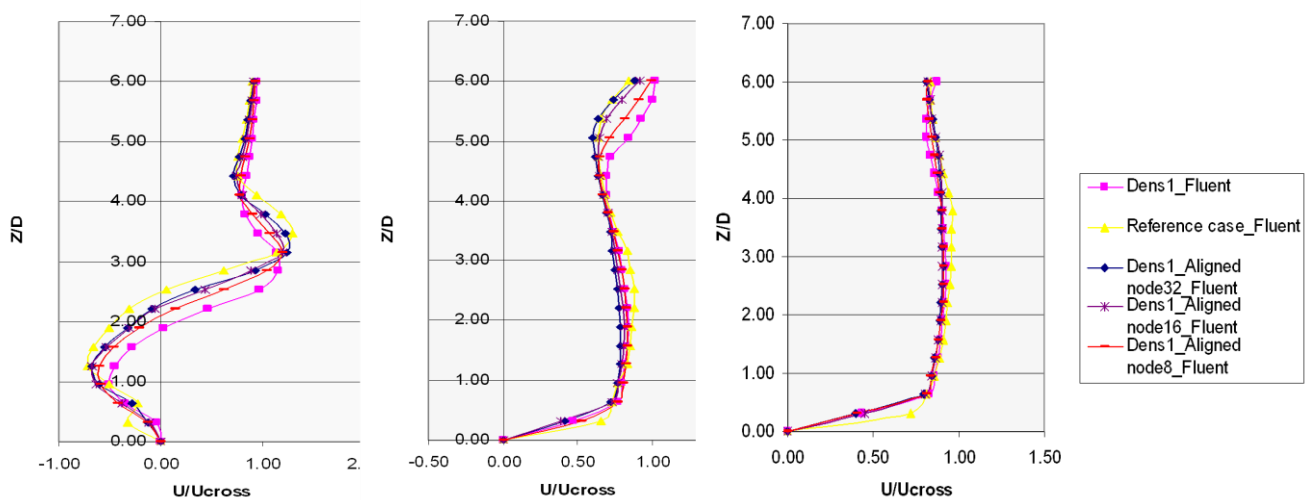


Figure 3.13 Profiles of velocity components U/U_{cross} at $X/D=1, 6$ and 10 , reference case vs. aligned nodes cases

As can be understood from Figure 3.13 the pipe wall resolution where the aligned nodes are more than 32 per 360° , give relatively better results. The differences in the region where the jet enters the channel are more noticeable than further down stream.

3.9 Case study III: Prism layers

The y^+ contour for case study II and reference case are shown in Figure 3.14. The results near the wall and especially at $X/D=1$ and near the jet entrance $Z/D < 1$, shows a significant discrepancy. That can be improved if the boundary layer is adjusted properly.

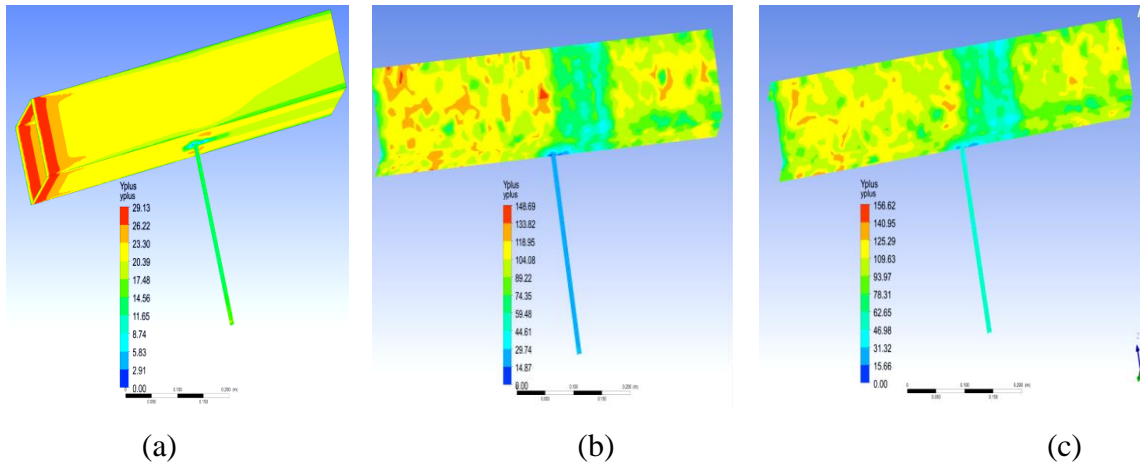


Figure 3.14 y^+ contour (a) Reference case, (b) case Study II 32 aligned nodes and (c) case Study II 16 aligned nodes

The wall resolution may have a significant effect especially where constant velocity is applied. The profile of velocity at the inlet of channel is illustrated schematically in figure below. The wall resolution can be improved by adding prism layers.

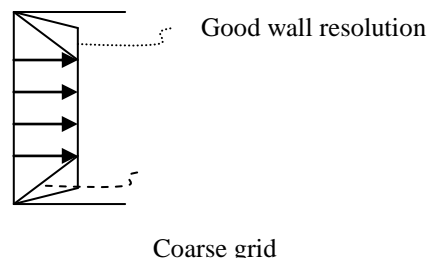


Figure 3.15 Velocity profile at the inlet of channel

3.9.1 Prism layers

Tetra meshing is not efficient for capturing shear or boundary layer physics. Prism mesh efficiently captures these effects near the surface while maintaining the ease and automation of Tetra mesh.

The smoothing is the most time consuming part, so for simple configurations, it is helpful to grow thicker layers and then split it to the desired number of layers.

Here the total height of prism layers is considered 0.5 mm. The effect of wall resolution is studied for cases with 16 and 32 aligned nodes around half nozzle pipe and with refined areas the same as the case study one.

At the first attempts 5 prism layers have been created. The prism mesh has been generated in a way that the first and last layer height was 0.03 mm and 0.2 mm respectively.

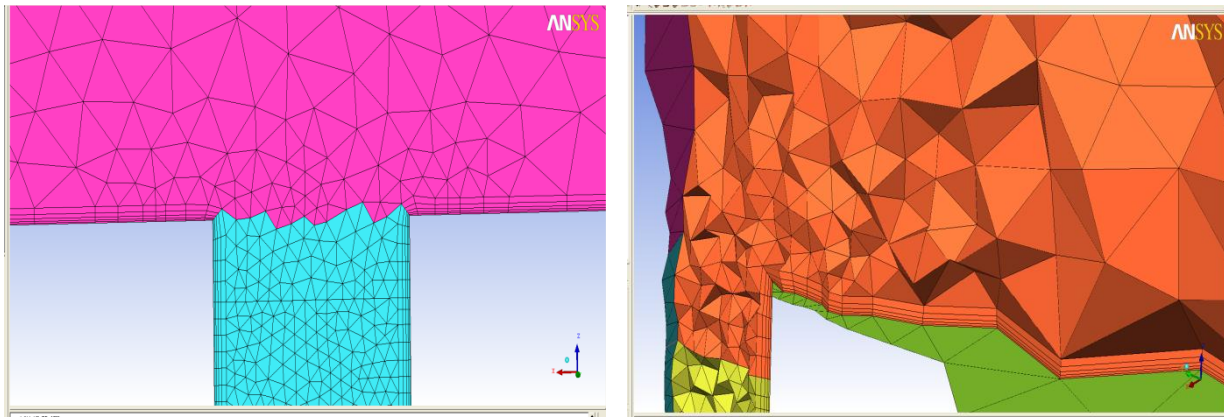


Figure 3.16 32 aligned nodes case with 5 layers prism

Also the prisms with same total height but less number of layers are implemented. The prism mesh has been generated in a way that the first layer height was 0.2 mm and second layer height was 0.3 mm.

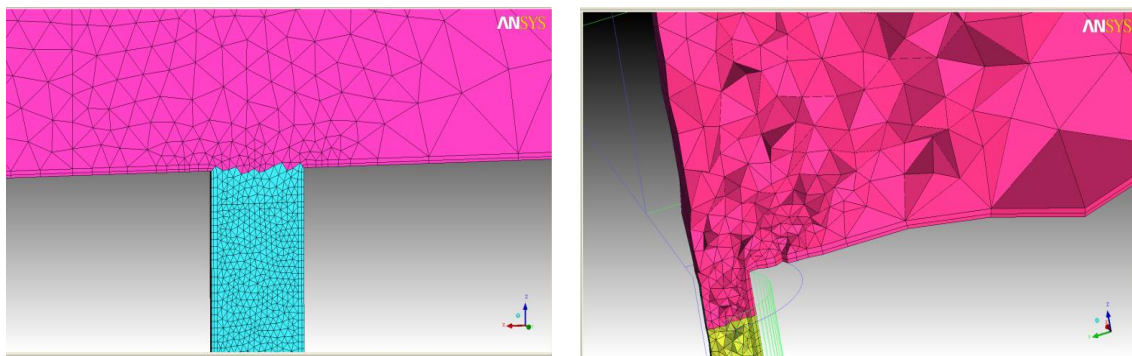


Figure 3.17 32 aligned nodes case with 2 layers prism

The grid specification for the cases with 32 aligned nodes per 180° and two and five prism layers is summarized in Table 3.7. The related data for the case with 16 aligned nodes per 180° are mentioned in Appendix.

Table 3.7 Case study III grid specification

	Dens1_aligned node32_prism 5l	Dens1_aligned node32_prism 2l
Number of cells	527,677	408,613
Mesh Type	Tetrahedral	Tetrahedral
Element size		
Refined region	1/4D	1/4D
Other region	1 D	1 D
Pipe wall region	1/32 D	1/32 D
Structure type	32 Aligned nodes per 180°	32 Aligned nodes per 180°
Blocking	0.16%	0.16%
Prism	5 layers	2 layers
Orthogonal quality	≥0.44	≥0.46

3.9.2 Results

As was expected, adding prism layers improved the results in the regions near the wall. As illustrated in Figure 3.18, Y plus has been decreased when prism layers have been added.

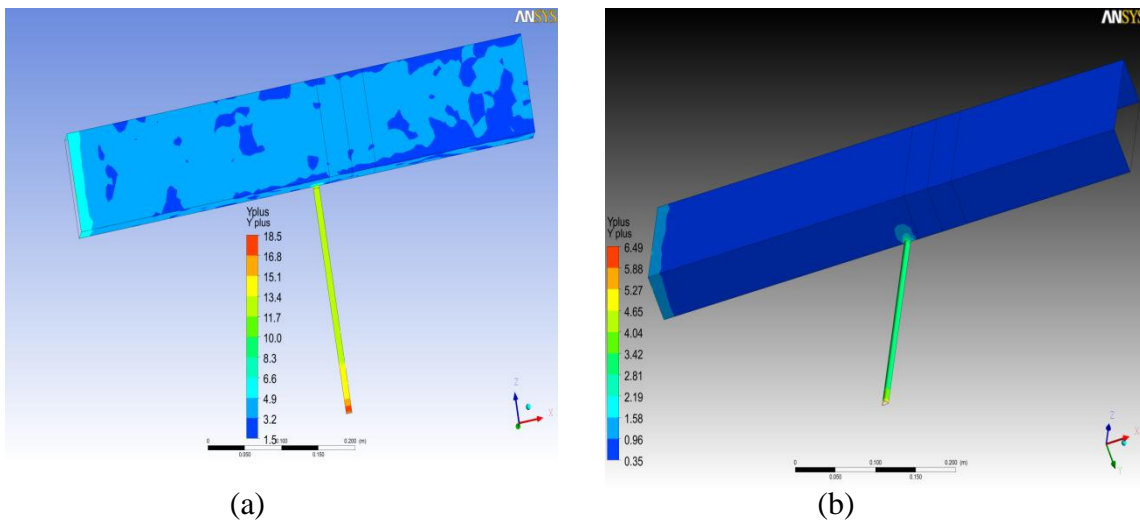


Figure 3.18 y^+ contour Case study III, 32 aligned nodes and (a) 2 prism layers (b) 5 prism layers

The velocity profile for the case with 32 aligned nodes around the half pipe, with and without prisms have been compared in Figure 3.19.

The velocity profile for the cases with prism layers are very close to the reference case. The difference between 5 and 2 prism layers are small, while the difference without any prisms is significant.

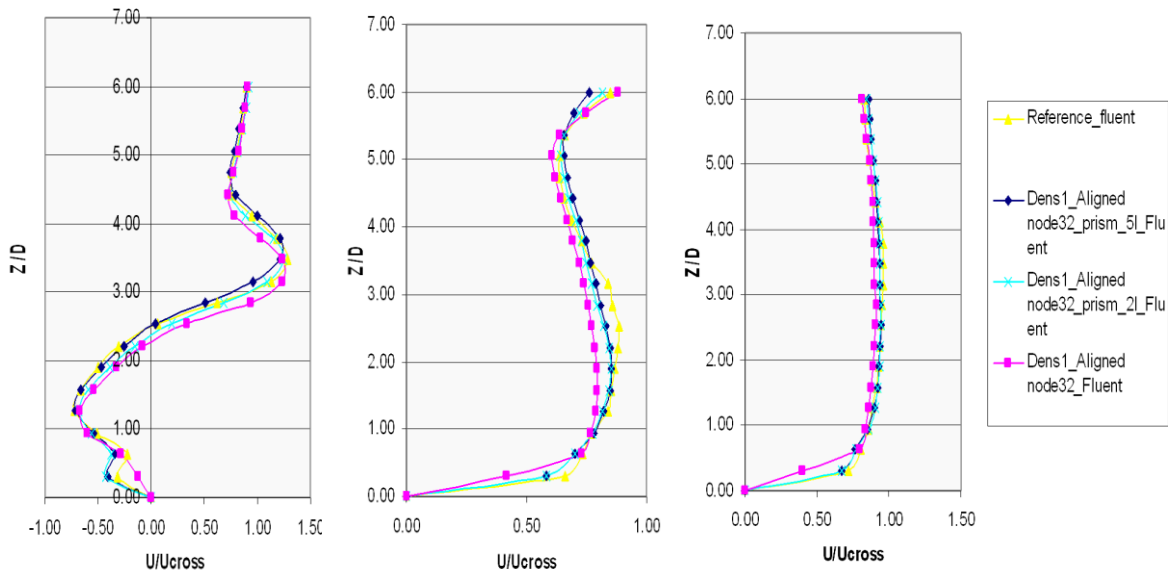


Figure 3.19 Profiles of velocity components U/U_{cross} at $X/D=1,6$ and 10 , Reference case vs. Case study II and III

3.10 Case study IV: without density box

According to the results in previous sections, the most effective strategy for achieving reliable results is implementing structured mesh for the pipe nozzle and adding prism layers. In case Study IV the case without density box but with structured grid in pipe nozzle, has been investigated.

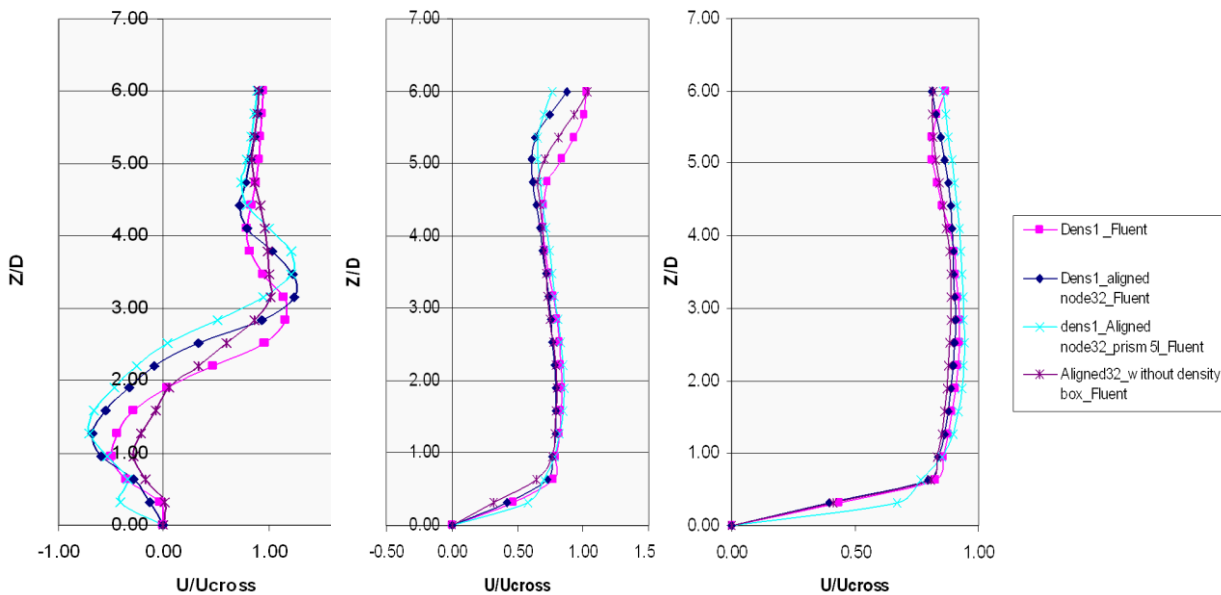


Figure 3.20 Profiles of velocity components U/U_{cross} at $X/D=1,6$ and 10 , Case study I, II, III and IV, Fluent

In Figure 3.20 the velocity profile for all type of case studies so far has been illustrated. As it can be seen in the figure refined areas have a weaker effect on velocity profile downstream. But in the area near the jet entrance refined regions are necessary and affect the accuracy of results significantly.

3.11 Grid independency:

Grid independency for case study III (the most accurate results) has been checked. The case with 64 aligned nodes per 360° and 5 prism layers, were refined more in order to check the grid dependency. For this purpose the region adaption capability in Fluent has been used. The case has been adapted in a way that all cells split once.

As is shown in Figure 3.21, the velocity profile is not changed significantly when the grid was refined, indicating negligible grid dependency.

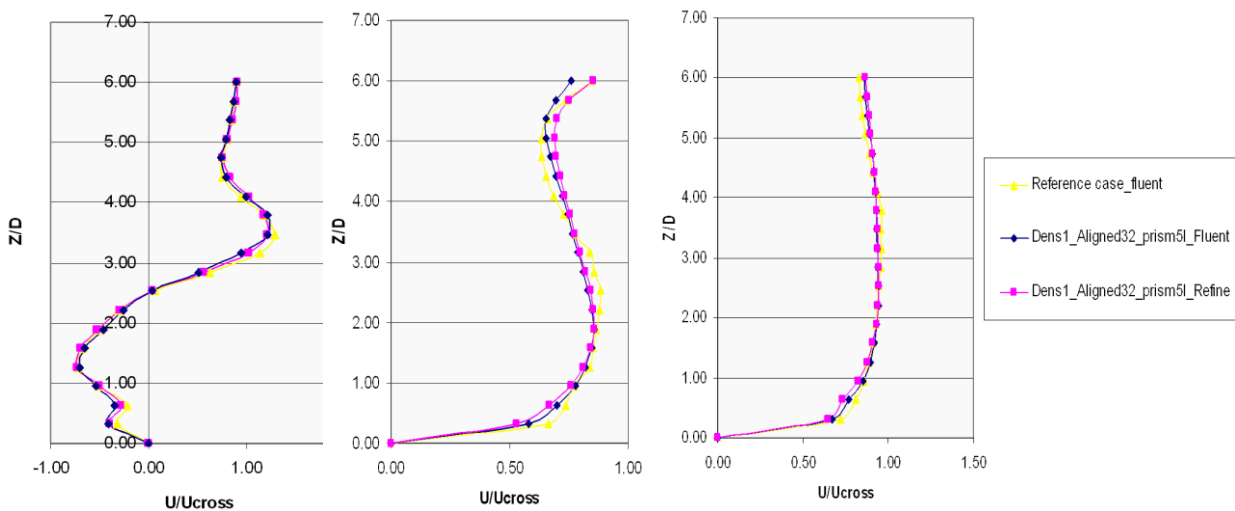


Figure 3.21 Profiles of velocity components U/U_{cross} at $X/D=1,6$ and 10 , grid independency, Fluent

Although the velocity profile is closed to grid independent, the dimensionless concentration (C) is still different for the grid with better resolution. Figure 3.22 shows the results for C field in the same positions where the velocity profile has been investigated.

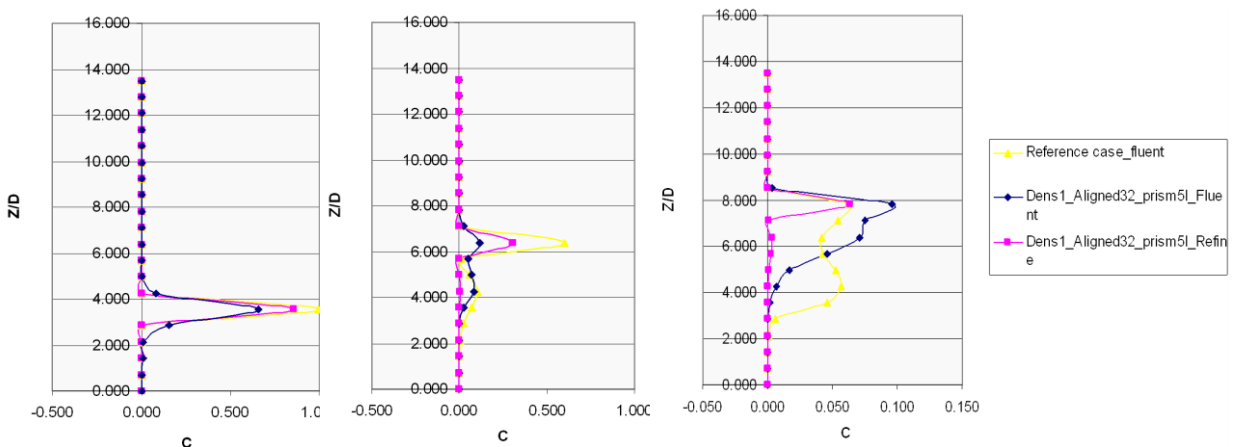


Figure 3.22 Dimensionless concentration at $X/D=1,6$ and 10 , grid independency, Fluent

The goal is to find a mesh strategy which is grid independent for both velocity profile and dimensionless concentration.

3.12 Case study V: grid independent solution for dimensionless concentration

The dimensionless concentration contour in the symmetry plane even for the case which has the best compatibility (32 aligned nodes per 180° with 2 prism layers) is not the same as the reference case¹. See Figure 3.23

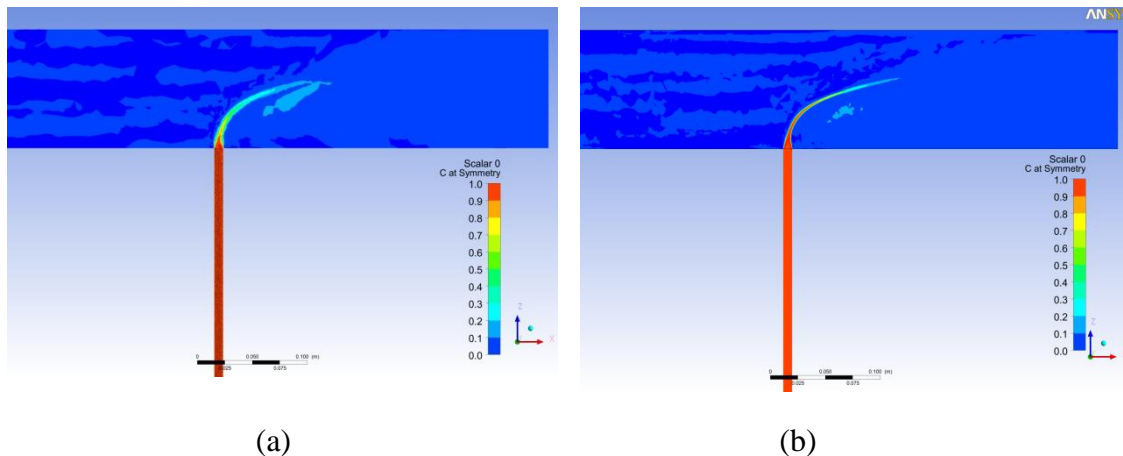


Figure 3.23 Dimensionless concentration contour at symmetry plane in (a) case study III, 32 aligned nodes per 180° and 2 prism layers (b) reference case

That might be because neither the reference case is grid independent. As shown in Figure 3.23 the mesh is not well resolved outside the main jet trajectory which may have an effect. Hence the grid independency of the reference case should be checked also. A region adaption for the whole reference domain was applied and all cells were split once. Unfortunately the attempt was not successful and the mesh quality decreased dramatically after adaption and therefore the solution didn't converge.

Since the grid independency of reference case is not proven in this thesis it has been attempted to find a grid independent solution for the studied cases. In case study V, the density boxes have been broader. Also the region where the jet enters to the channel has been refined more by adding an extra cylindrical density box along the pipe nozzle until one fourth of channel height (with cell size $1/4 D$).

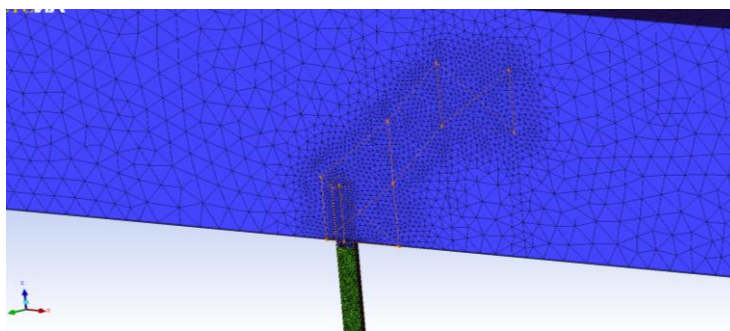


Figure 3.24 Case study V, density boxes

¹ That was because Fluent user defined tracer equation do not include turbulence effect but this was not known at this stage!

The new grid specification is mentioned in Table 3.8.

Table 3.8 Case study V grid specification

Number of cells	483,136
Mesh Type	Tetrahedral
Element size	
Refined region	1/2D, 1/4D
Other region	1 D
Pipe wall region	1/32 D
Structure type	64 Aligned nodes per 360°
Blocking	0.16%
Prism	2 layers
Orthogonal quality	≥ 0.4

In order to avoid unnecessary cell refinement, gradient adaption with the curvature method has been used. The gradient of the dimensionless concentration improved by 37% (from $8e^{-5}$ to $5e^{-5}$) The primary number of marked cells was 11818 and with dynamic adaption every 20 iterations during the solution, the number of cells in the grid increased to 727,849 cells that means 50% more than the case without adaption. Most of the refined cells as can be seen in the figure below are located in edge of the jet trajectory and further downstream.

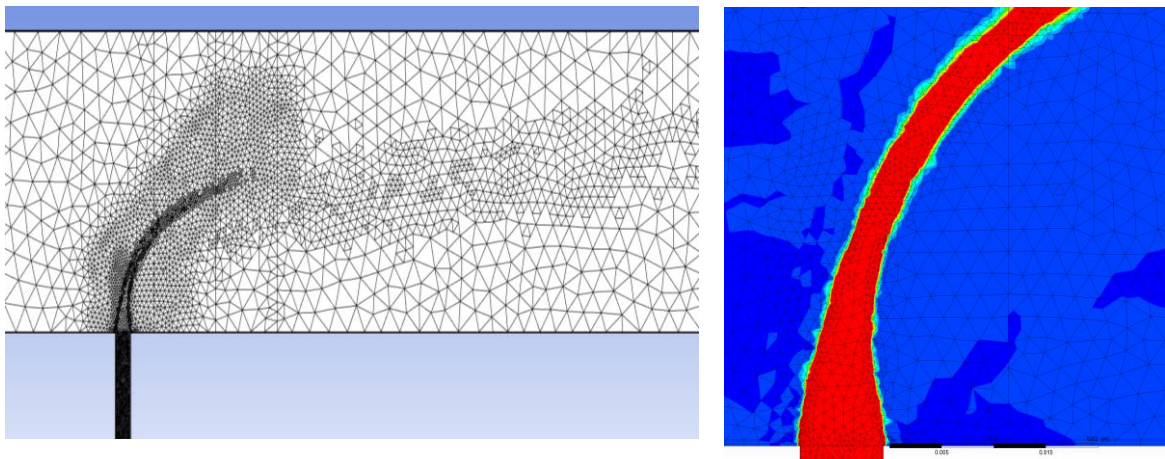


Figure 3.25 Case study V, Grids with first level of gradient adaption

Table 3.9 Grid specification

Number of cells	727,849
Mesh Type	Tetrahedral
Gradient of dimensionless concentration	$\leq 5e^{-5}$
Structure type	64 Aligned nodes per 360°
Blocking	0.16%
Prism	2 layers
Orthogonal quality	≥ 0.19

The results shown in Figure 3.26 compare the dimensionless concentration profiles in the cases with and without grid adaption.

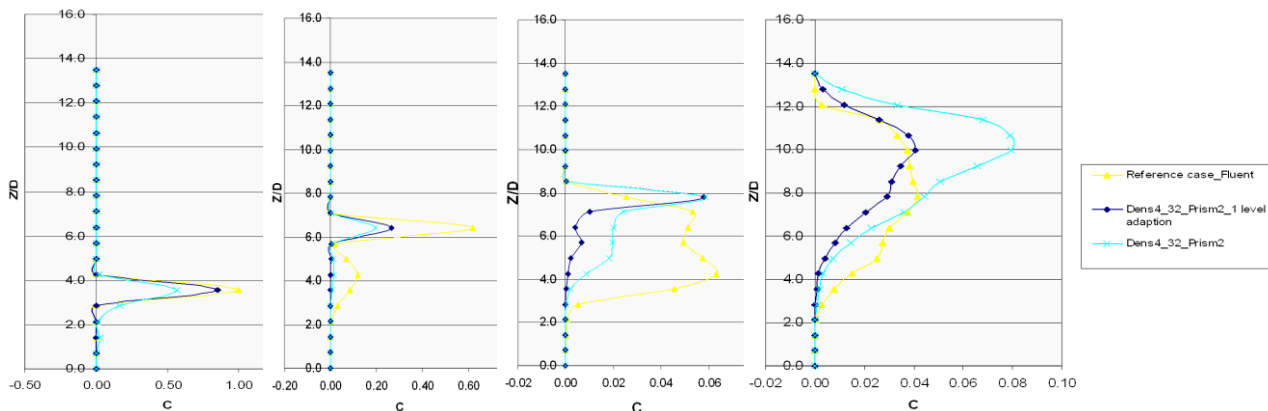


Figure 3.26 Gradient adaption effect at $X/D=1,6,10$ and outlet

The gradient adaption is performed in order to decrease the gradient of C as much as possible. Unfortunately the efforts for decreasing 50% and more weren't successful and the level of adaption was stopped at 43% decrease in gradient of C .

In this level of adaption, 643 cells were marked primarily and once the convergence achieved the number of cells raised. This procedure continued until there were 53% more cells in the computational domain as compared to the original case before adaption.

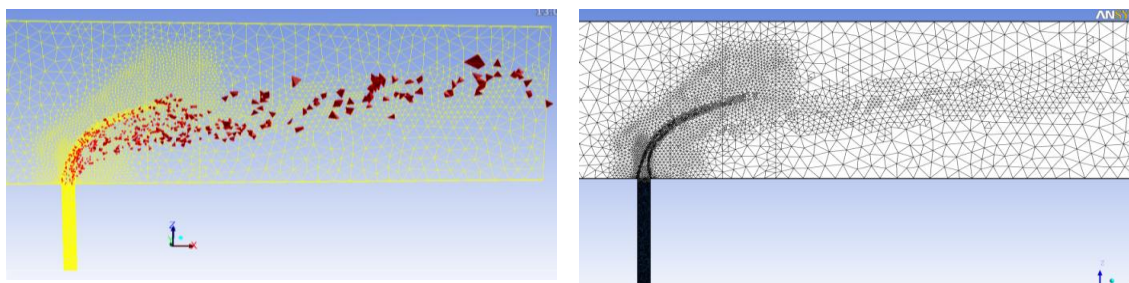


Figure 3.27 Case study V, Grids with second level of gradient adaption.

Table 3.10 Grid specification

Number of cells	738,314
Mesh Type	Tetrahedral
Gradient of dimensionless concentration	$\leq 4.5 e^{-5}$
Structure type	64 Aligned nodes per 360°
Blocking	0.16%
Prism	2 layers
Orthogonal quality	≥ 0.19

In Figure 3.28 it can be seen that the predicted C contours at the symmetry plane for both level of adaption are improved.

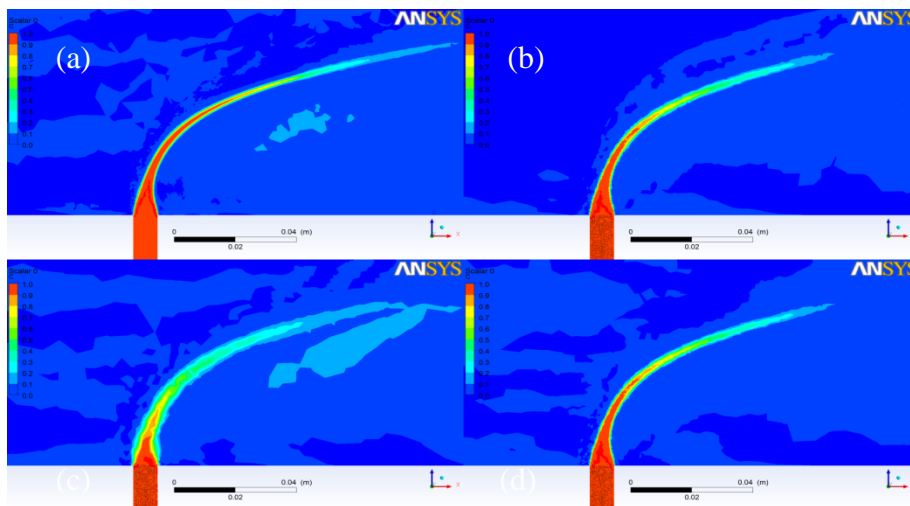


Figure 3.28 Dimensionless concentration at symmetry plane, (a) reference, (b) adaption level $5e^{-5}$, (c) adaption level $4.5e^{-5}$ and (d) without adaption.

In order to investigate the grid independency of the dimensionless concentration, region adaption is applied to both of gradient adapted cases. The region adaption splits all cells twice as compared to the non-adapted original mesh. In this method those cells that were already split twice or more during the dynamic adaption would not be split in this step. The number of cells after region adaption increased to around 5 million.

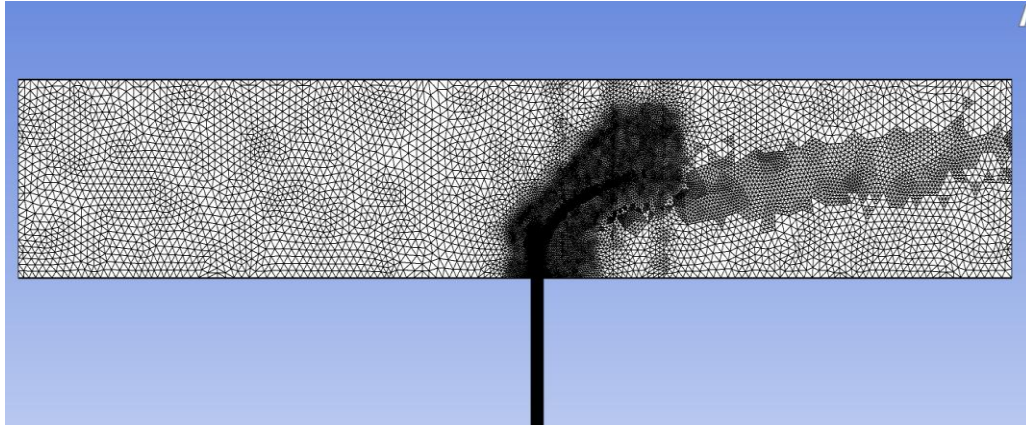


Figure 3.29 Study V grid, with gradient adaption and region adaption.

Figure 3.30 compares the velocity profiles at different cross sections for different grids. The profiles that are shown here belong to the gradient adapted case (about 700,000 cells), region adapted case (about 5 million cells) and reference case (around 6 million cells). It can be observed that the velocity profiles show a grid independent behaviour as they are in good agreement with each other.

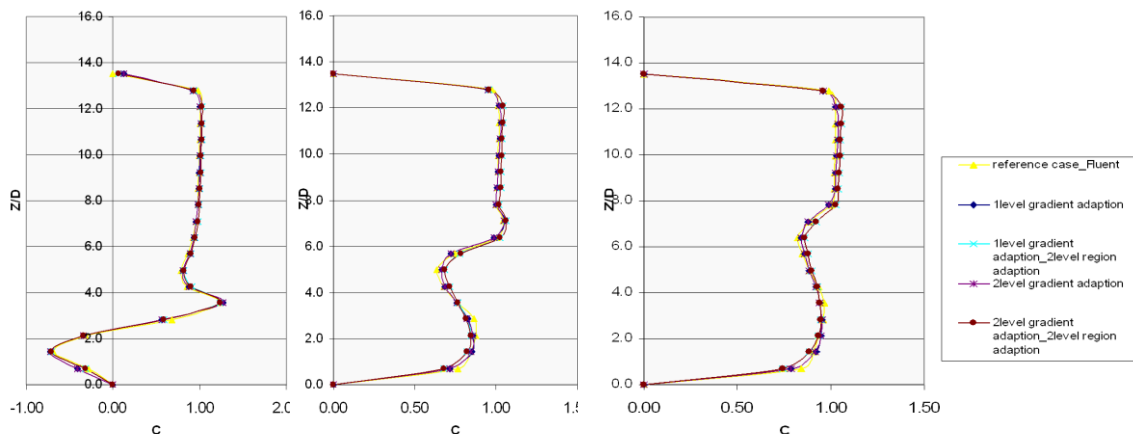


Figure 3.30 Velocity profile grid independency at $X/D=1,6$ and 10

Although the velocity field is grid independent, the dimensionless concentration field shows a grid dependent behavior. This is shown in Figure 3.31.

Only in the region close to the jet entrance a grid independent behavior can be observed. The reason could be the sufficient grid refinement in this region that does not change anymore with further grid adaption. The grid dependency of the dimensionless concentration profile at the regions close to $x/D > 6$ implies that the results are not reliable in these regions.

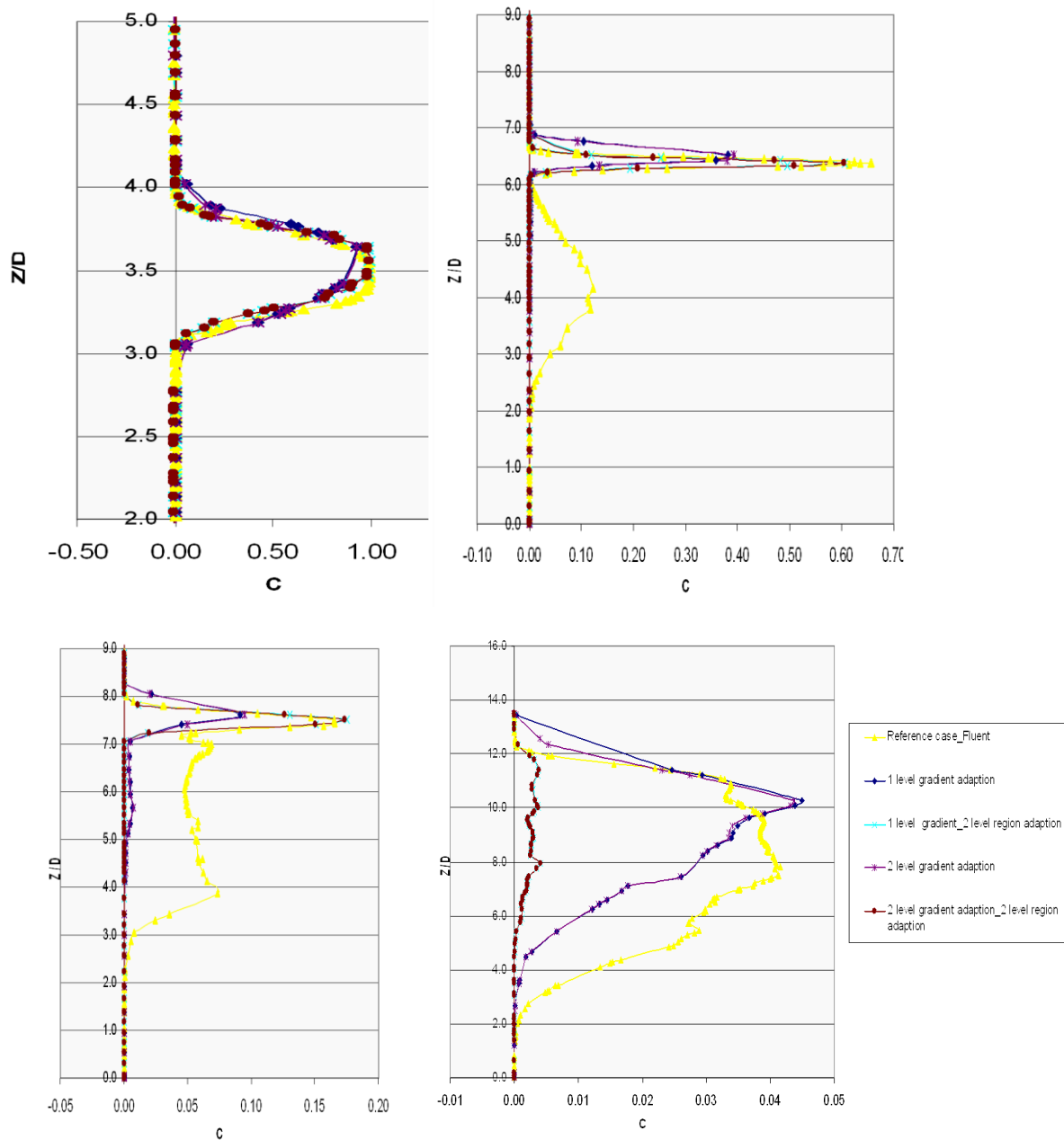


Figure 3.31 Dimensionless concentration at $X/D=1, 6, 10$ and outlet for different adaption methods and levels vs. reference case.

Comparison of the dimensionless concentration results for the SIT case, the case without adaption and the case with gradient and region adaption shows the same trends, see Figure 3.32. So the C contour at plane $x=D$, $x=6D$ and $x=10D$, for the mentioned cases was investigated. The C contour for the adapted case in Figure 3.33 shows a laminar behavior in a turbulent flow! In other words the Fluent user defined tracer equation does not take the turbulence effects into account.

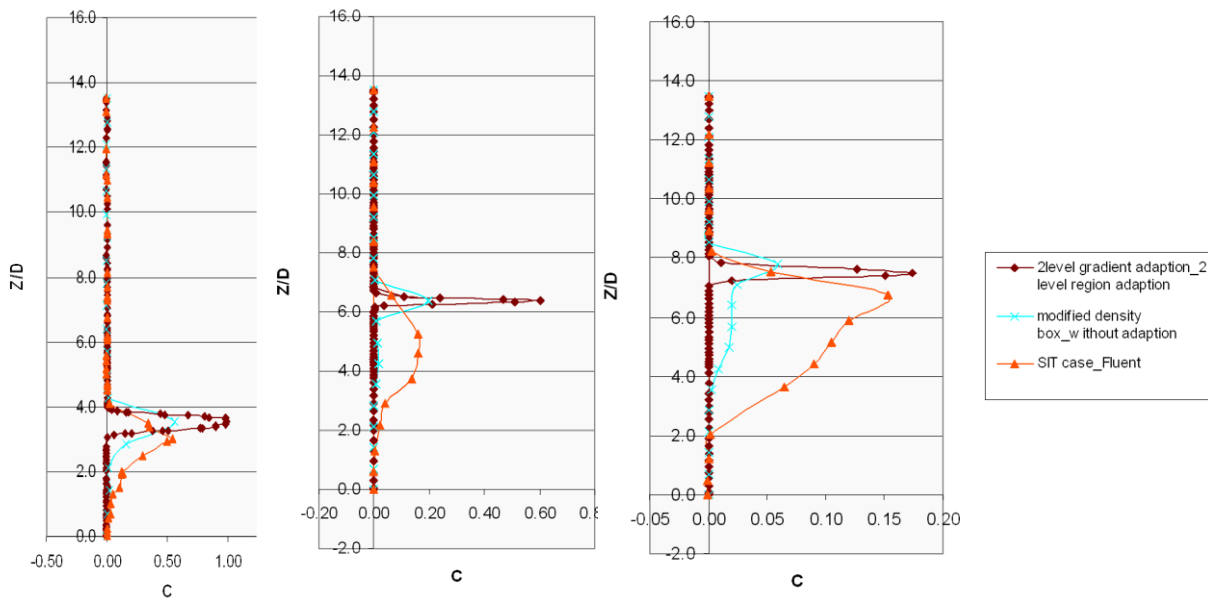


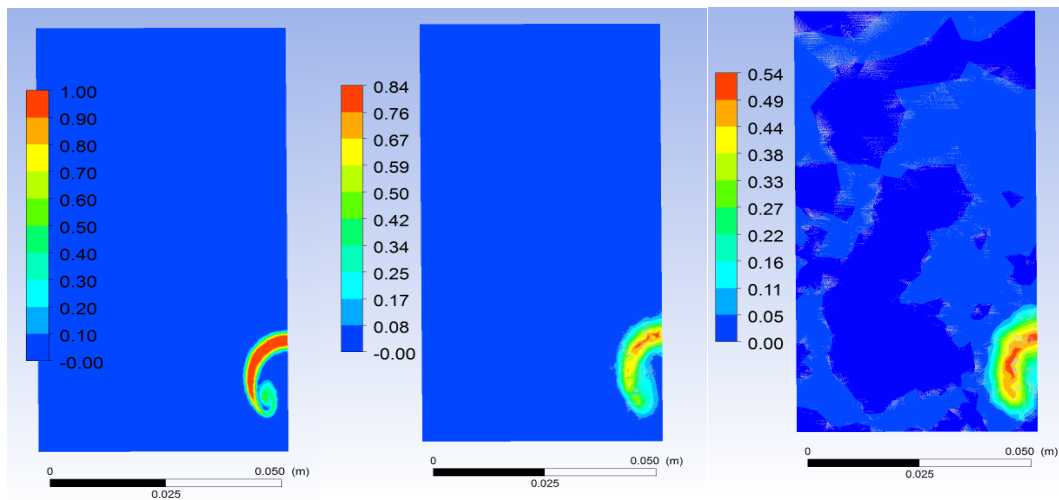
Figure 3.32 Dimensionless concentration at $X/D=1,6$ and 10 , SIT case, none adapted case, Adapted case

$X=1D$

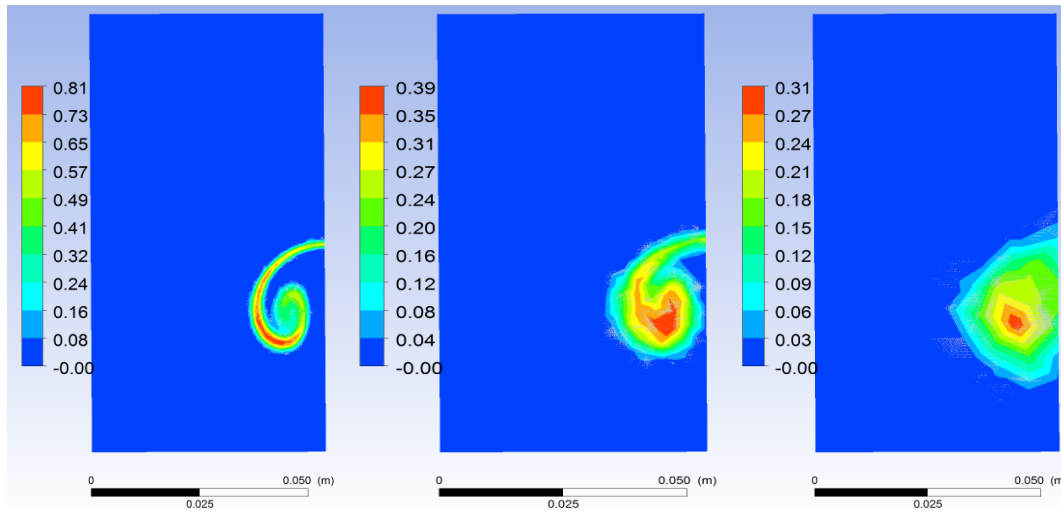
Adapted case

None adapted case

SIT case



X=6D



X=10D

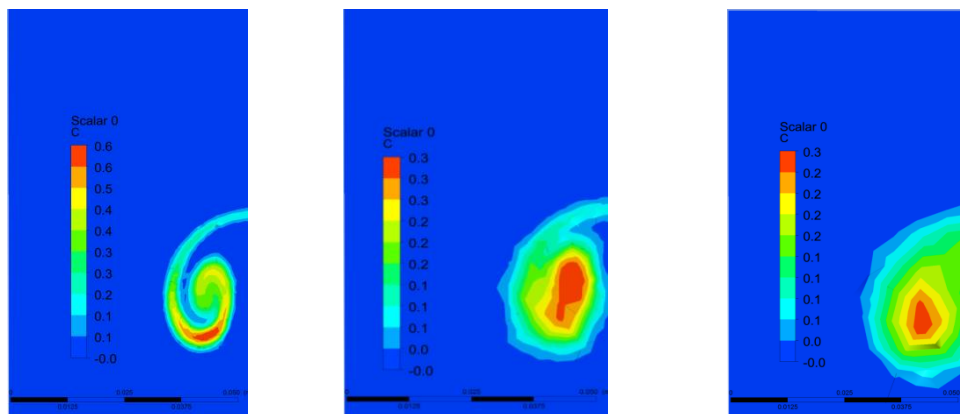


Figure 3.33 Dimensionless concentration profile and contour

Lack of turbulence terms in the tracer equation was not known until this stage. The species model in Fluent takes the turbulence effects into account for concentration with default Schmidt number 0.7. Since in this thesis it was tried to follow the same setup (for boundary condition and material definition) as for the reference case, user defined scalar was used.

As results show the grid independency of the dimensionless concentration can not be judged when turbulence effect is eliminated in user defined scalar. This should be investigated in the future works.

3.13 Fluent versus CFX

As it was mentioned in section 3.5 there is a discrepancy between the Fluent and CFX results. Here the effect of channel length is investigated. The channel length in both downstream and upstream direction is elongated approximately 4 times to make sure that the flow is fully developed.

The velocity profile at $x/D=1$ for the case V (without adaption) with longer channel is compared to the same case with original channel length in Figure 3.34.

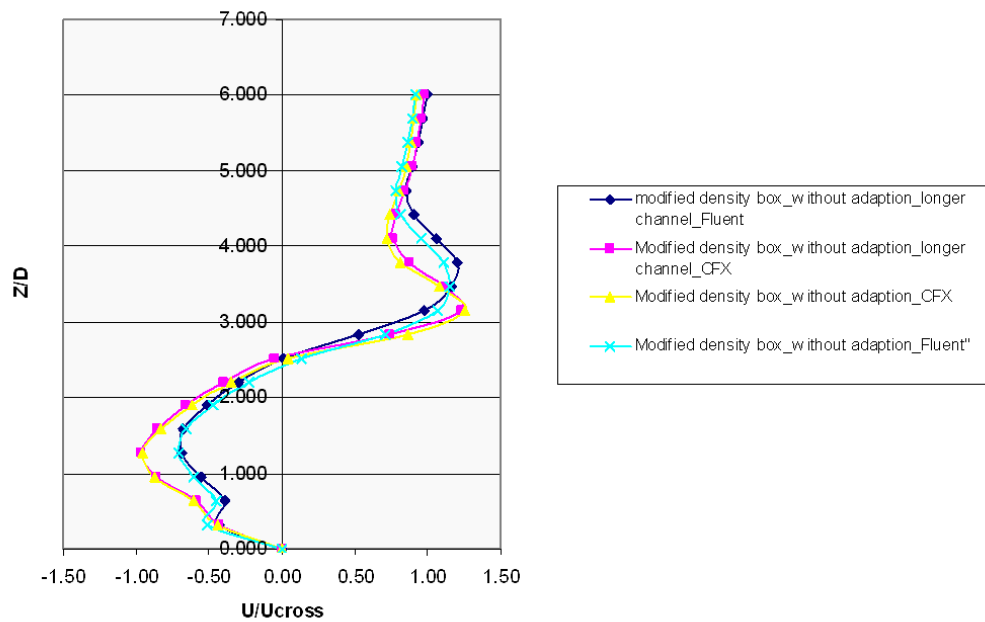


Figure 3.34 Velocity profile at $X=D$, CFX vs. Fluent

As can be seen in the figure the effect of channel length is very small and still the difference between CFX and Fluent results is considerable and should be investigated in the future works.

4 Conclusion:

A recommended mesh strategy in order to achieve accurate results while avoiding unnecessary mesh refinements is summarized as follows.

The most important step is to create refined region properly. According to the results, density boxes which are created through the jet flow lead to better results. Since creating such density boxes in a real burner with more than one jet and swirling flow is not easy, the region where the jet enters the channel should be refined at least. The recommended regions and cell sizes is depicted in the following figures.

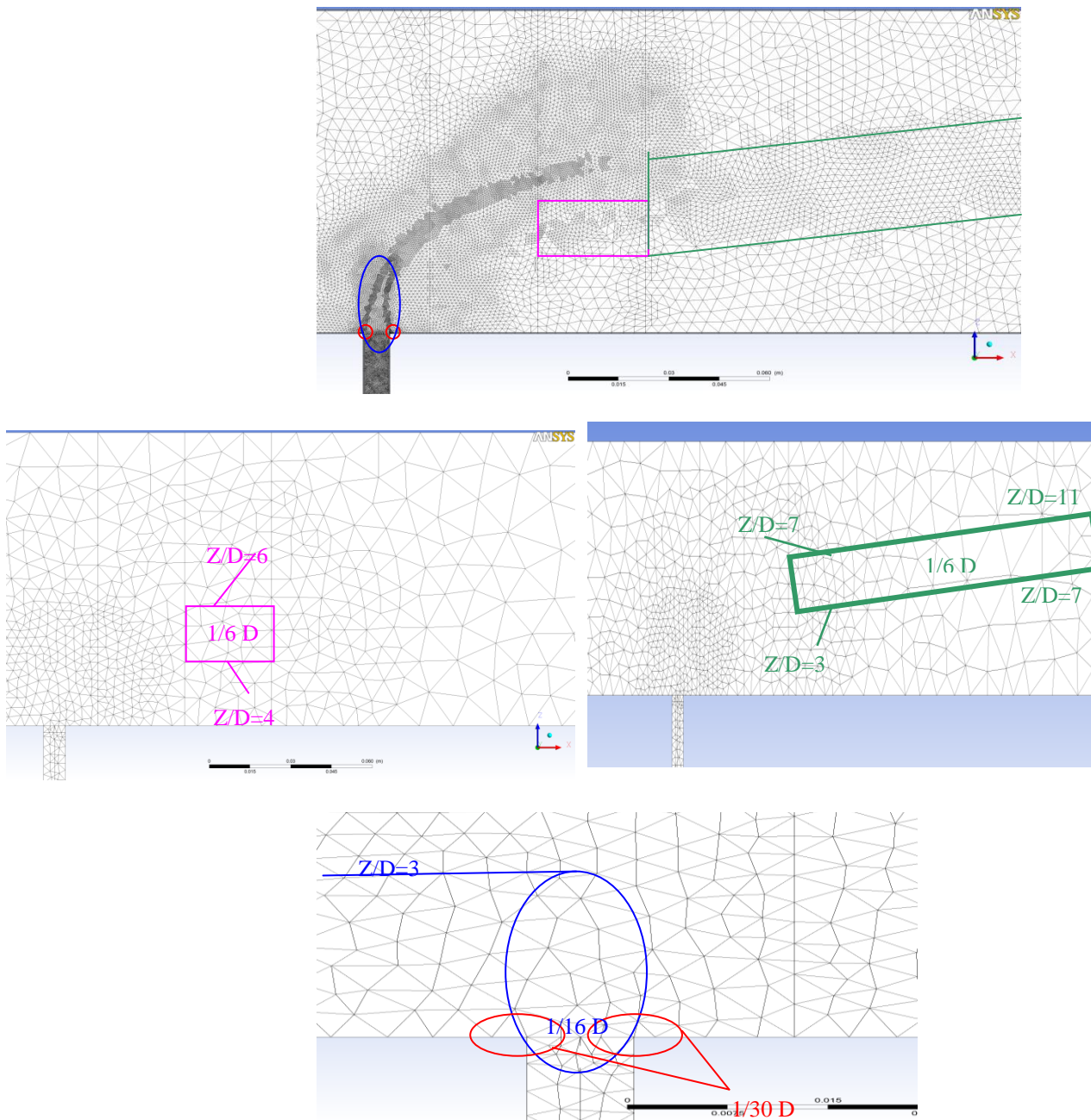


Figure 4.1 Recommended mesh

Also structured grid along the pipe wall with suitable amount of aligned nodes (at least 32 aligned nodes per 360°) reduces the blocking and consequently improves the accuracy of the results. Channel wall resolution also affected the accuracy of the results especially in the region close to the downstream of the jet pipe. Adding prism layers in these regions can improve the results considerably.

Grid independency:

The acquired results suggest the grid independency for velocity profile but the grid independency of the dimensionless concentration is still a question mark. Nevertheless using adaption to refine the grid is a good method to improve the accuracy of the results with no need for unnecessary cells refinements in the grid generating program.

5 Future work:

There is a discrepancy between the Fluent and CFX results. This needs to be further investigated. Differences may stem from symmetry plane in half model or may be due to differences of standard and realizable k- ϵ models in CFX and Fluent, respectively. Using the same turbulence model such as k- ϵ or SST, might fix this problem.

Only steady state simulations are performed in this work. Transient simulations should be performed and compared to the steady state solutions.

Grid independency of CFX results should be checked. Since it was difficult to adapt the mesh or refine it in ICEMCFD, other grid generation soft wares (ex. Hypermesh or Centaur) may be used to do the mesh refinement.

In this work a tracer was employed to predict the concentration field. Since this tracer was independent from the turbulence field it was impossible to acquire a grid independent concentration field. Therefore it is suggested that the grid dependency of the concentration field to be investigated by solving the actual conservation of concentration equation. This can only be achieved by having another species such as methane at the nozzle jet as the running fluid.

Also the recommended mesh strategy should be applied to the SGT-800 burner and the grid independency of the results should be verified.

6 References

ANSYS (2010): ANSYS CFX Theory Guide, Version 13.0, 2010

ANSYS (2010): ANSYS Fluent Theory Guide, Version 13.0, 2010

Barhaghi, DG; CFD-guidelines, 1CS97054 ed A, Siemens Industrial Turbomachinery AB, 2010

Bruneflod S. (2010): Flow simulations of an axisymmetric two dimensional 3rd generation DLE burner. Master Thesis. Department of Applied Physics and Mechanical Engineering Division of Fluid Mechanics, Luleå University of Technology, Luleå, Sweden, 2010

Davidson L. (2003): An introduction to Turbulence models. Department of Thermo and Fluid Dynamics, Chalmers University of Technology, Publication no. 97/2, Göteborg, Sweden, 2003.

Galeazzo F., Donnert G., Habisreuther P., Zarzalis N., Valdes R., Krebs W. (2010): Measurement and simulation of turbulent mixing in a jet in Cross flow. ASME Turbo Expo 2010: Power for Land, Sea and Air, GT2010-22709, June 2010

Larsson E. (2009): Flow simulations of a gas turbine burner using CFX and OpenFOAM. Master Thesis. Department of Applied Mechanics, Division of Fluid Dynamics, Chalmers University of Technology, Publication no. 2009:07, Göteborg, Sweden, 2009.

Navrotsky V., Strömberg L., Uebel C. (2009): SGT-800 gas turbine continued availability and maintainability improvements. POWER-GEN, Asia 2009 , Bangkok, Thailand, October 2009

Pope S. (2000): Turbulent flows. Cambridge University press, Cambridge, United kingdom

Websites:

Siemens website www.siemens.com

<http://www.innovative-cfd.com/turbulence-model.html/>

<http://www.lr.tudelft.nl/nl/actueel/laatste-nieuws/artikel/detail/colloquium-n-khatri/>

Appendix

This appendix includes two parts. In part A, the effect of wall resolution is investigated for an extra case in Fluent. And in the part B the CFX results can be found.

A. Fluent

The results for the case study III with 16 aligned nodes per 180° and 2 prism layers have shown in figures below:

Table A.1 Grid specification

	Dens1_aligned node16_prism 2l
Number of cells	185,706
Mesh Type	Tetrahedral
Element size	
Refined region	1/2D
Other region	1 D
Pipe wall region	1/16 D
Structure type	16 Aligned nodes per 180°
Blocking	0.64%
Prism	2 layers
Orthogonal quality	≥ 0.3

By adding the prism layers wall resolution and consequently the results have improved.

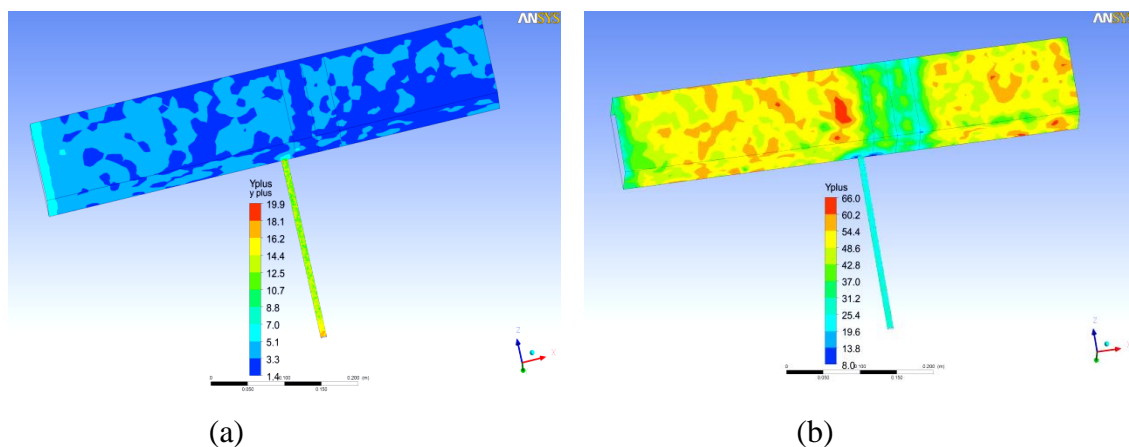


Figure A.1 y^+ contour Case study III, 16 aligned nodes and (a) 2 prism layers (b) without prism

In the Figure A.2 the velocity profile for the cases with 16 and 32 aligned nodes per 180° , with and without prism are compared to the reference case.

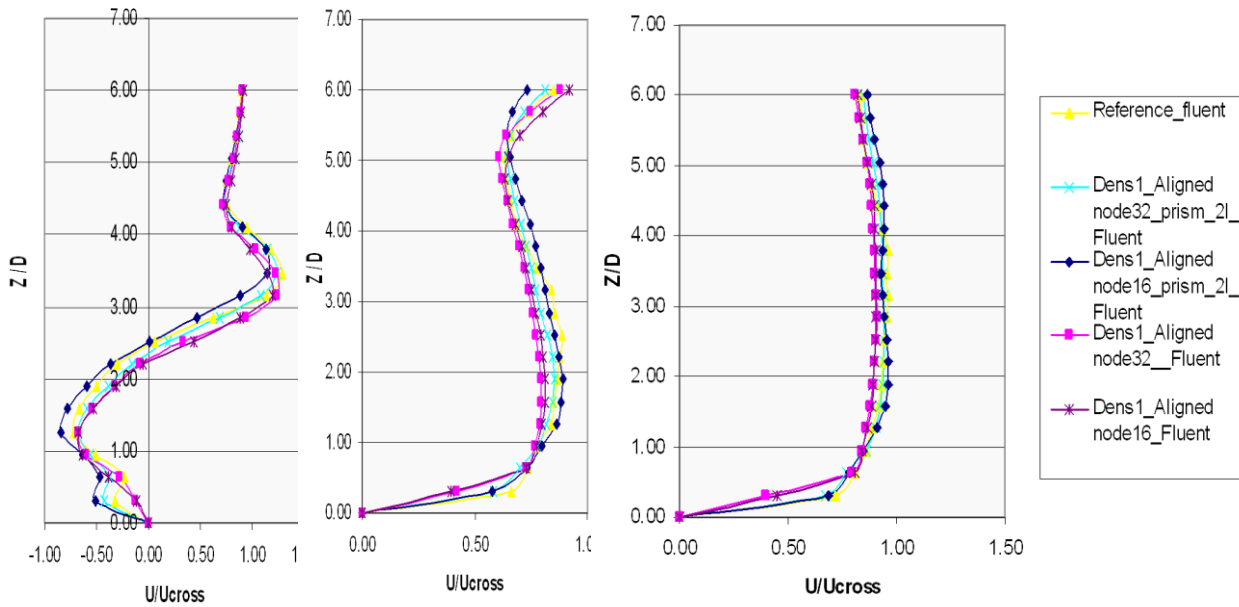


Figure A.2 Profiles of velocity components U/U_{cross} at $X/D= 1, 6$ and 10 , Reference case vs. Case study III

As can be seen in the figure the prism layers improve the results in the case with 32 aligned nodes more than the case with 16 aligned nodes.

B. CFX results

In this thesis all the steps except adaption are performed by CFX too. Here the CFX results can be found.

B.1 SIT case:

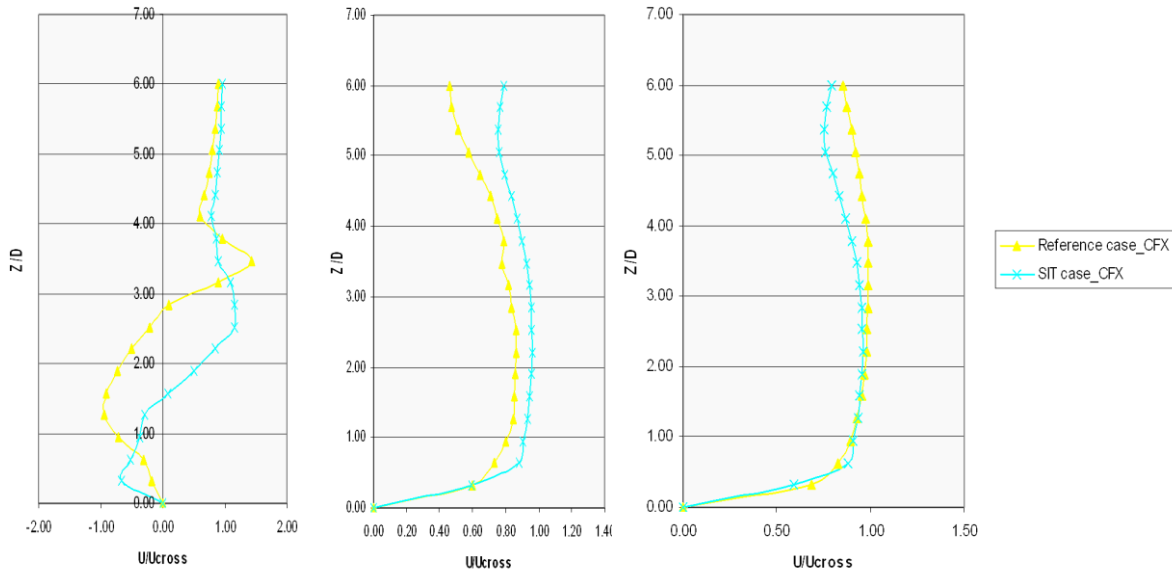


Figure B.1 Profiles of velocity components U/U_{cross} at $X/D=1, 6$ and 10 , Reference case vs. SIT using CFX

B.2 Case study II: Structured grid in nozzle pipe

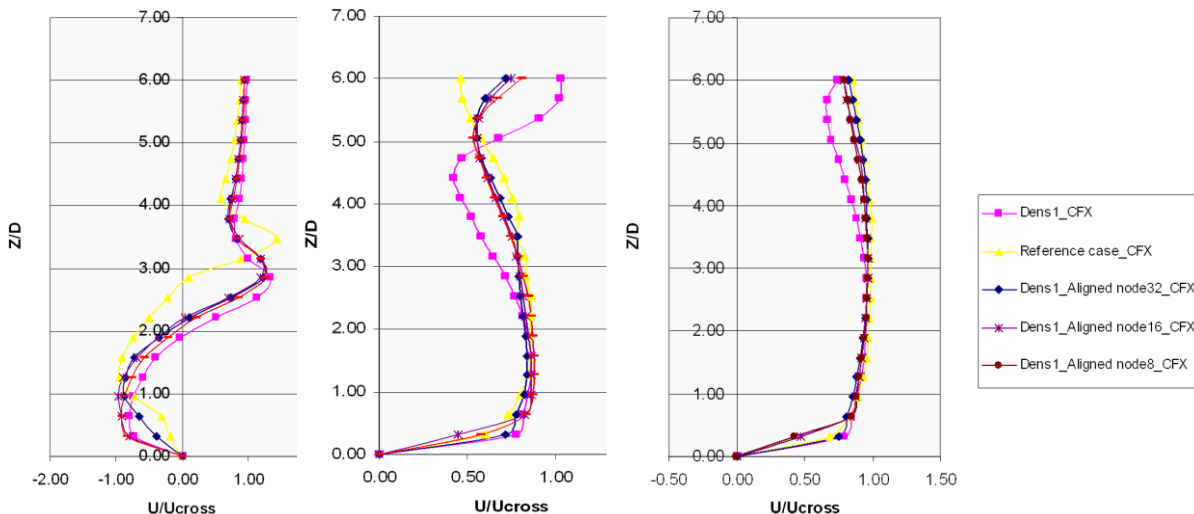


Figure B.2 Profiles of velocity components U/U_{cross} , at $X/D=1, 6$ and 10 , reference case vs. aligned nodes cases using CFX

B.3 Case study III: Prism layers

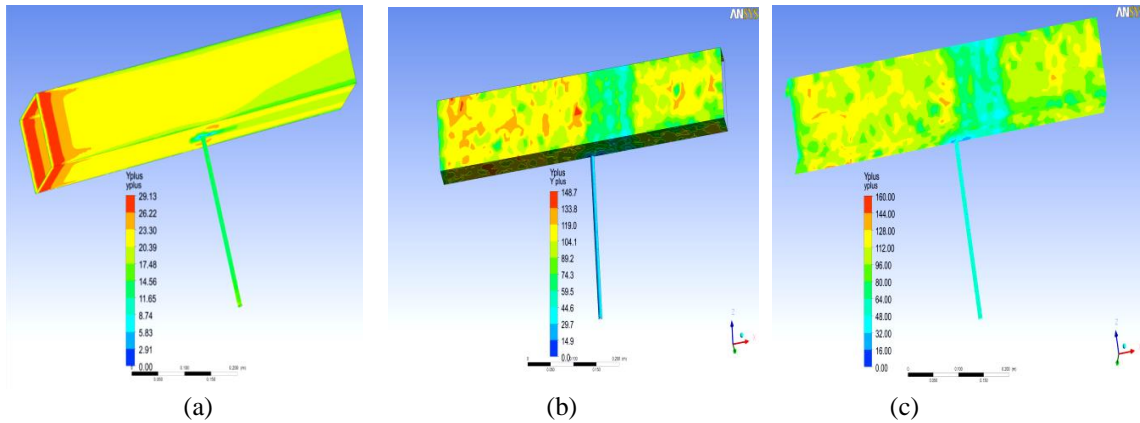


Figure B.3 y^+ contour (a) Reference case, (b) case Study II 32 aligned nodes and (c) case Study II 16 aligned nodes using CFX

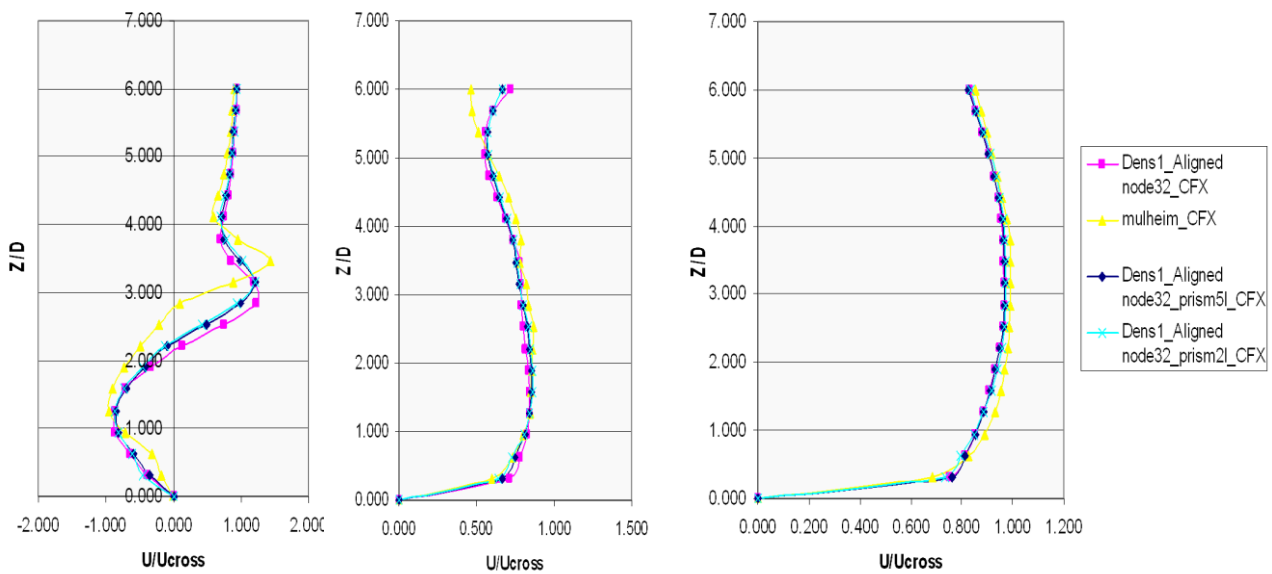


Figure B.4 Profiles of velocity components U/U_{cross} at $X/D=1, 6$ and 10 , Reference case vs. Case study II and III

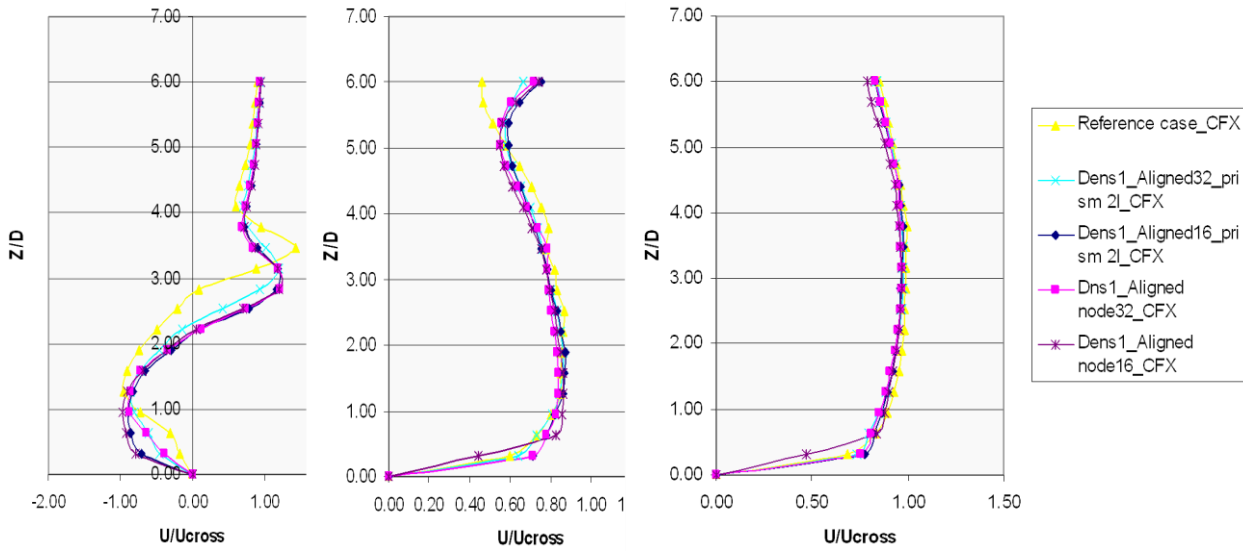
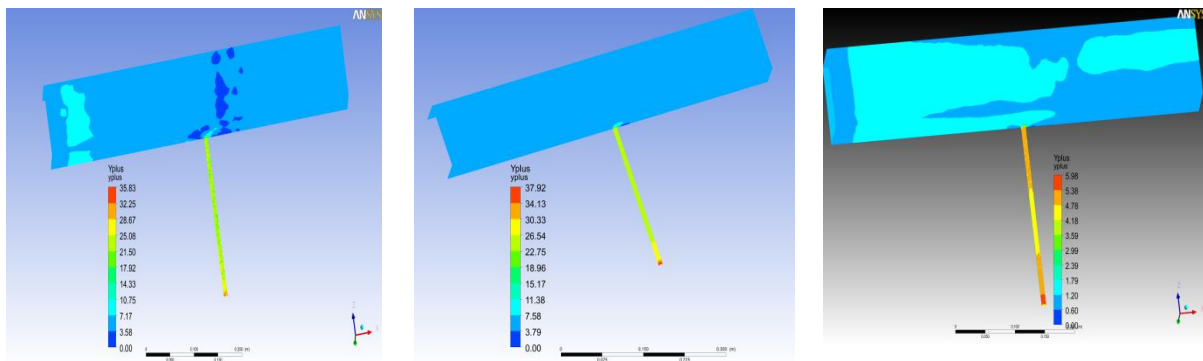


Figure B.5 Profiles of velocity components U/U_{cross} at $X/D=1, 6$ and 10 , Reference case vs. Case study III, CFX



(a)

(b)

(c)

Figure B.6 y^+ contour (a) case Study III 16 aligned nodes with 2prism layers, (b) case Study III 32 aligned nodes with 2 prism layers and (c) case Study III 32 aligned nodes with 5 prism layers using CFX

B.4 Case study IV: Without density boxes

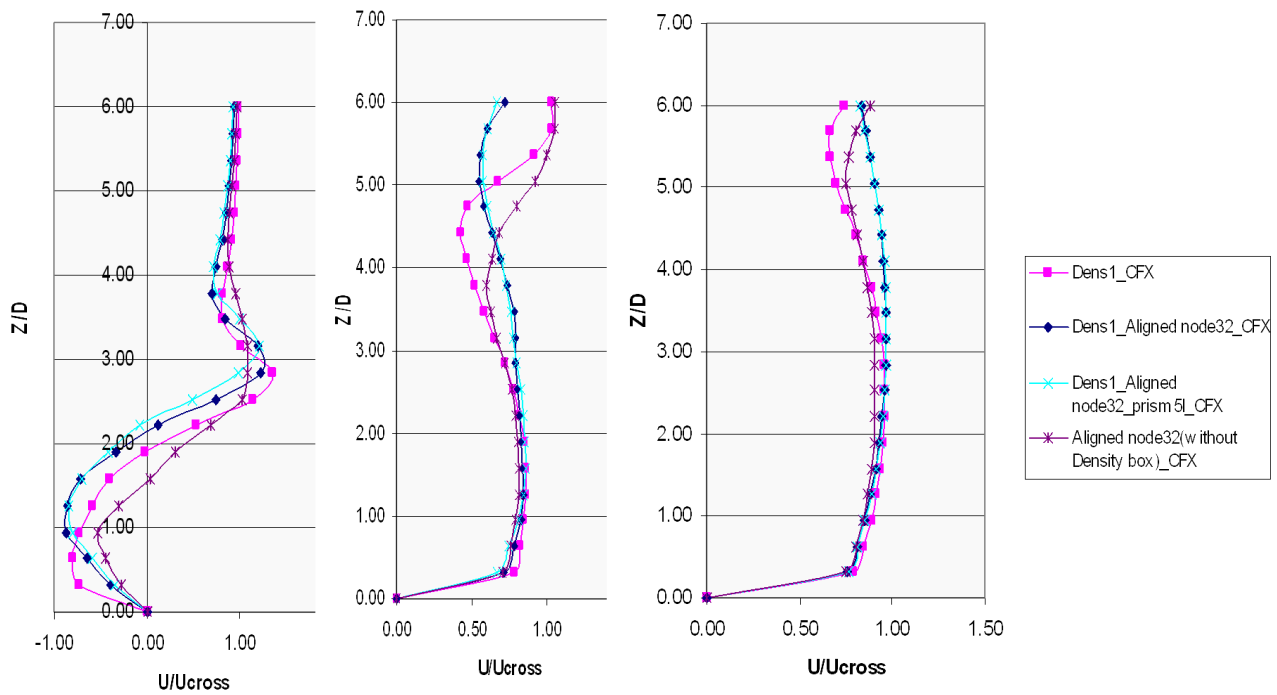


Figure B.7 Profiles of velocity components U/U_{cross} at $X/D = 1, 6$ and 10 , Case study I, II, III and IV, CFX

B.5 Grid independency

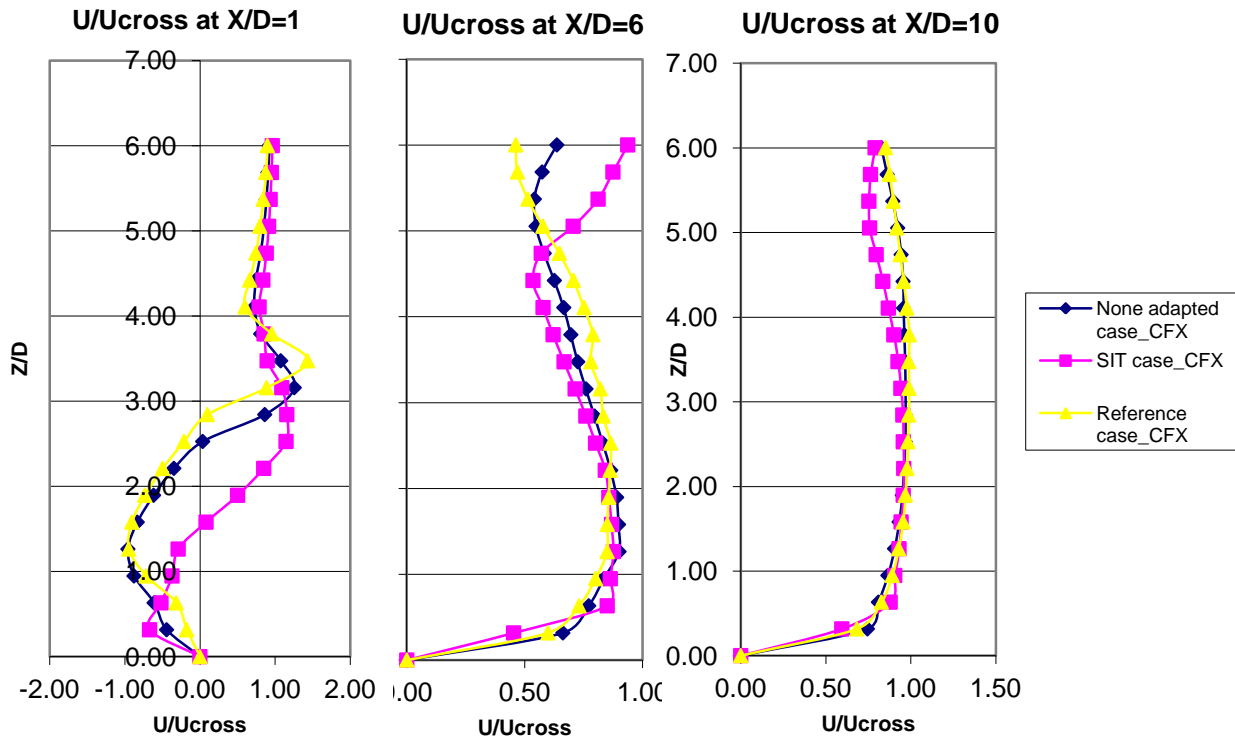


Figure B.8 Velocity profile at $X/D= 1, 6$ and 10 , SIT case, none adapted case, Reference case, CFX

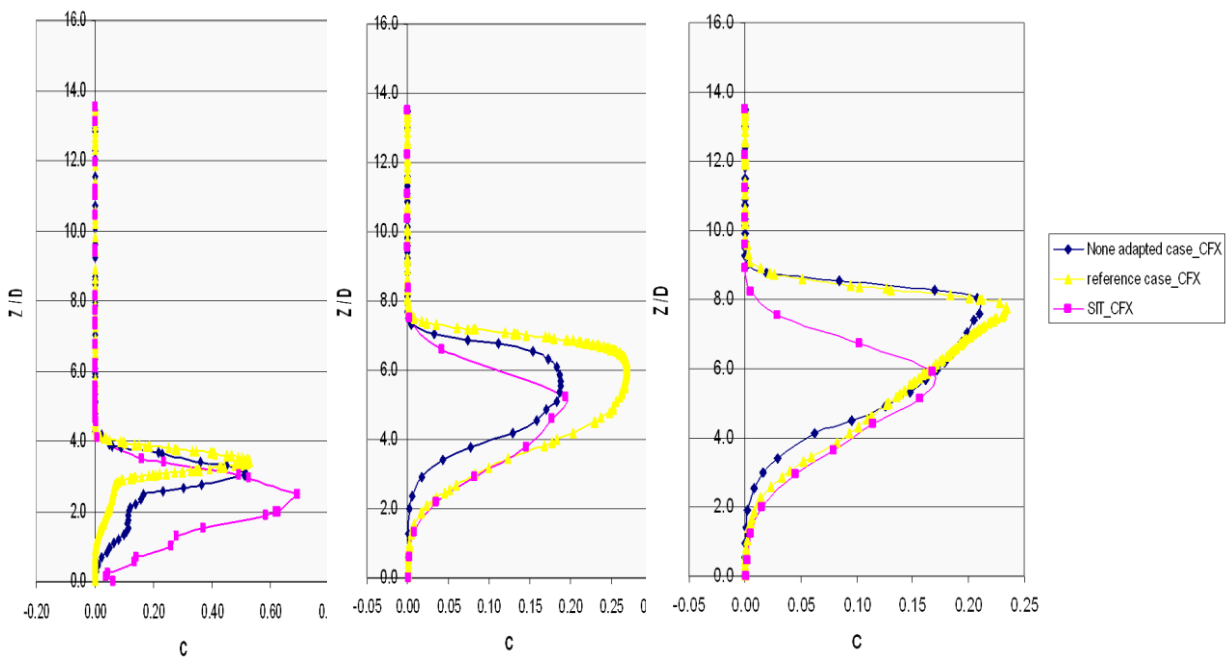


Figure B.9 Dimensionless concentration at $X/D= 1, 6$ and 10 , SIT case, none adapted case, Reference case, CFX

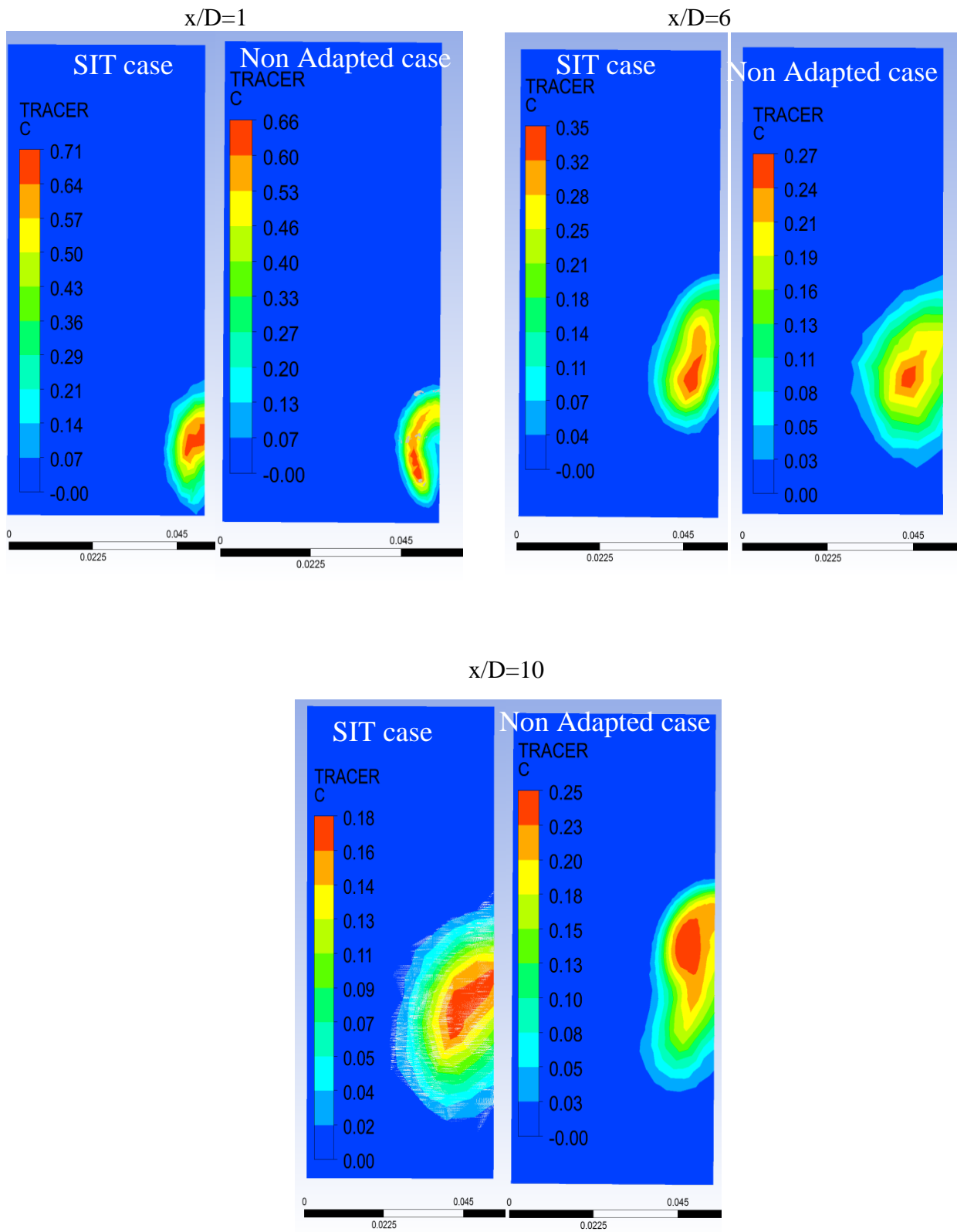


Figure B.10 Dimensionless concentration contour, CFX